Title

P23H opsin knock-in mice reveal a novel step in retinal rod disc morphogenesis.

Journal

Human Molecular Genetics, 23(7)

Authors

Sakami, Sanae

Kolesnikov, Alexander

Kefalov, Vladimir

et al.

Publication Date

2014-04-01

DOI

10.1093/hmg/ddt561

Peer reviewed

Human Molecular Genetics, 2014, Vol. 23, No. 7 **1723–1741**
doi:10.1093/hmg/ddt561
Advance Access published on November 7, 2013

P23H opsin knock-in mice reveal a novel step in retinal rod disc morphogenesis

Sanae Sakami[1], Alexander V. Kolesnikov[2], Vladimir J. Kefalov[2] and Krzysztof Palczewski[1,*]

[1]Department of Pharmacology, School of Medicine, Case Western Reserve University, 10900 Euclid Avenue, Cleveland, OH 44106, USA and [2]Department of Ophthalmology and Visual Sciences, Washington University School of Medicine, St Louis, MO 63110, USA

Received August 12, 2013; Revised and Accepted November 5, 2013

Retinal rod photoreceptor cells have double membrane discs located in their outer segments (ROS) that are continuously formed proximally from connecting cilia (CC) and phagocytized distally by the retinal pigmented epithelium. The major component of these rod discs, the light-sensitive visual pigment rhodopsin (Rho), consists of an opsin protein linked to 11-*cis*-retinal. The P23H mutation of rod opsin (P23H opsin) is the most common cause of human blinding autosomal dominant retinitis pigmentosa (adRP). A mouse model of adRP with this mutation (*Rho*$^{P23H/+}$) shows low levels of P23H opsin protein, partial misalignment of discs and progressive retinal degeneration. However, the impact of mutant P23H opsin on the formation of abnormal discs is unclear and it is still unknown whether this mutant pigment can mediate phototransduction. Using transretinal ERG recordings, we demonstrate that P23H mutant Rho can trigger phototransduction but *Rho*$^{P23H/P23H}$ rods are ~17 000-fold less sensitive to light than *Rho*$^{+/+}$ rods and produce abnormally fast photo-responses. By analyzing homozygous *Rho*$^{P23H/P23H}$ knock-in mice, we show that P23H opsin is transported to ciliary protrusions where it forms sagittally elongated discs. Transmission electron microscopy of postnatal day (PND) 14 *Rho*$^{P23H/+}$ mouse retina revealed disordered sagittally oriented discs before the onset of retinal degeneration. Surprisingly, we also observed smaller, immature sagittally oriented discs in PND14 *Rho*$^{+/-}$ and *Rho*$^{+/+}$ mice that were not seen in older animals. These findings provide fundamental insights into the pathogenesis of the P23H mutant opsin and reveal a novel early sagittally aligned disc formation step in normal ROS disc expansion.

INTRODUCTION

Rod photoreceptor cells of the vertebrate retina have a unique membrane-rich structure at the cilium, the rod photoreceptor cell outer segment (ROS), consisting of over 800 intracellular membrane discs. The disc double membranes house the most abundant ROS membrane protein, opsin (1–3), which not only plays an essential role in ROS disc formation but also is associated with photoreceptor degeneration when expressed at abnormally high levels or it is absent (4–6). Rhodopsin (Rho) is a G protein-coupled receptor consisting of an apo-protein opsin linked to a vitamin A-derived chromophore (11-*cis*-retinal). Its activation upon photoisomerization of 11-*cis*-retinal to all-*trans*-retinal initiates the neuronal signaling responsible for dim-light vision (7,8).

The P23H opsin is the most common cause of human autosomal dominant retinitis pigmentosa (adRP) (15–18% of all adRP cases in the USA) (9,10). P23H opsin accumulates in the endoplasmic reticulum (ER) of different cultured cells (11,12) and up-regulates proapoptotic unfolded protein response markers of the ER in transgenic P23H opsin animals (13–15). Thus, it has been hypothesized that P23H opsin can cause retinal degeneration via ER stress (13,16). Others proposed that proteasome overload is a stress factor that causes retinal degeneration (17). However, accumulation of P23H opsin in the ER was not detected in several other P23H opsin animal models (18,19). Among such transgenic models, the knock-in *Rho*$^{P23H/+}$ mouse best mimics the genetic background and pathological progression of human adRP with the P23H opsin mutation (20). It has been estimated that the P23H opsin level could be as low as 1–10% of WT opsin. The opsin and its mutant do not accumulate in the ER of the inner segments of knock-in *Rho*$^{P23H/+}$ mice, raising the question of how such a small amount of P23H opsin could cause rod photoreceptor cell death. Despite studies of multiple cell culture and animal models, it is still unclear whether regenerated P23H opsin can

*To whom correspondence should be addressed. Tel: +1 2163684631; Fax: +1 2163681300; Email: kxp65@case.edu

support phototransduction and if its signaling properties affect retinal degeneration (9,12,14,21–38). Therefore, we compared photoresponses of retinas from P23H opsin homozygous mice with those from WT and heterozygous mice.

Defective formation of ROS has been tested as another factor potentially responsible for retinal degeneration in mice carrying the P23H opsin mutation. Two competing models were proposed for ROS disc formation. First, transmission electron microscopy (TEM) analysis of ROS proximal to the connecting cilia (CC) has revealed vesicles and folding of the plasma membrane, suggesting that new discs are formed by evaginations of the plasma membrane (39). Alternatively, new discs could be formed by fusion of vesicles (40,41). Mutations or lack of glutamic acid-rich proteins, the β-subunit of the rod cGMP-gated channel, retinitis pigmentosa-1 and prominin 1 each result in sagittally aligned elongated discs (42–44). A small number of sagittally oriented elongated discs can be also found in the mouse model of adRP with P23H opsin ($Rho^{P23H/+}$) (20). Here, we show that sagittally oriented rod discs in mice are formed not only by P23H opsin but also by Rho in the retina of young $Rho^{+/+}$ mice. Our results identify a new early step in normal disc formation with positioning that provides insights into why abnormal discs are sagittally aligned. In addition, we found that in homozygous ($Rho^{P23H/P23H}$) mice, P23H Rho can activate the phototransduction cascade with low efficacy to produce abnormally rapid photoresponses.

RESULTS

P23H opsin forms abnormal discs

We sought to determine whether P23H opsin is directly involved in abnormal disc formation by investigating disc structures in homozygous P23H opsin knock-in mice ($Rho^{P23H/P23H}$). First, we analyzed postnatal day (PND) 14 $Rho^{P23H/P23H}$ retinas with fluorescence microscopy. Surprisingly, we observed the opsin signal concentrated in needle-like structures or dots at the top of inner segment or within the distal inner segment layer. To evaluate whether these structures were abnormal ROS, we examined them with double immuno-staining. The needle-shaped opsin staining at the top of IS co-localized with prominin 1, a marker for the proximal ROS and all of cone outer segment (COS) (Fig. 1D), but not with calreticulin, an ER marker (Fig. 1F) or GORASP 2, marker of the Golgi apparatus (Fig. 1F). To further evaluate the needle-like structures observed in $Rho^{P23H/P23H}$ retina, we employed plastic sections followed by TEM. Histological staining (toluidine blue) of plastic sections clearly showed abnormal outer segment structures in $Rho^{P23H/P23H}$ retinas (Fig. 1J). TEM sections from the same eye revealed normal stacks of discs (likely derived from cone photoreceptors) (Fig. 1L and N, white arrow), the ciliary protrusion (CP) (Fig. 1N, CP) and packs of elongated discs (Fig. 1L and O, black arrows). Typically, a pack of elongated discs was surrounded by retinal pigmented epithelium (RPE) microvilli (Fig. 1O, RM), suggesting active phagocytosis of elongated discs at this age (PND14). As a control, $Rho^{+/+}$ retinas were analyzed (Fig. 1A, C, E, G, I, K and M). Note that microscopy conditions that permitted visualization of the 1D4 signal in $Rho^{P23H/P23H}$ (Fig. 1B) resulted in saturation of the OS signal and less intense staining in both the IS and ONL in $Rho^{+/+}$ retinas (Fig. 1A). To better understand the observed elongated discs in $Rho^{P23H/P23H}$ retina, we next turn to PND12 mice.

TEM was used to analyze disc formation at PND12. At this stage, photoreceptors are immature in mice of all genetic backgrounds, and retinal degeneration in $Rho^{P23H/P23H}$ mice is still relatively mild. Thin retinal sections revealed that $Rho^{+/+}$ mice already formed stacks of discs (Fig. 2A). However, in retinal sections from $Rho^{P23H/P23H}$ mice, many rod cells had CPs rather than discs (Fig. 2B). Although we found rare disc structures in $Rho^{P23H/P23H}$ mice, these discs were elongated and abnormally oriented (Fig. 2C, ⇧). Also, we found disc-like structures inside IS (Fig. 2C, ⬆), which are structurally similar to discs, but did not have disc rims and the distance between their membranes was not uniform. Similar to Rho (45), P23H opsin predominantly localized in the CPs of $Rho^{P23H/P23H}$ mice (Fig. 2E, ⇧). By using immuno-EM, we found that the elongated and abnormal discs also contained P23H opsin (Fig. 2F, ⇧). Low magnification clearly showed predominant localization of P23H opsin in the elongated and abnormal discs (Fig. 3). Thus, P23H opsin was transported to the distal ends of CC where it mostly formed CPs or a small number of sagittally oriented discs in $Rho^{P23H/P23H}$ mice.

The above observations were confirmed by several specific findings revealed in TEM serial sections (Fig. 4). The fifth sections of CP structures exhibited internal globate vesicles and tubules (Fig. 4B) which accumulated in the middle of CPs (Fig. 4C, green ⇧ and 4F, inset). Tubules and vesicles were not detected in a CC. Instead, tubules and vesicles showed evidence of endocytosis involving a deep plasma membrane invagination (Fig. 4C, inset). The typical double membrane visualized in serial sections clearly indicates that these were discs rather than tubular structures (Fig. 4D and E, blue ⇧). To identify whether these elongated discs were or were not located in inner segments, we analyzed more TEM images of $Rho^{P23H/P23H}$ mice and found that elongated discs were connected to CPs (Fig. 4G and H, *inset*). But we failed to identify any clear connections between a CC and CPs linked to elongated discs (Fig. 4G and H, pink CC), because in such images, a CC adjacent to CPs appeared only as a transversely-cut structure (Fig. 4G and H, pink CC). This observation indicates that elongated discs had to be laterally connected to CPs as shown by hypothetical diagrams of photoreceptor cells (Fig. 4).

Because rod membranes could be confused with cone membrane structures not affected directly by the P23H opsin, we employed immuno-EM to discriminate rod from cone membranes. As expected, characteristic discs of cone photoreceptor cells were not labeled with the rod opsin antibody (Fig. 5), indicating that the abnormal discs were not derived from cones.

Sagittally oriented discs are formed before rod degeneration occurs in immature $Rho^{P23H/+}$ mice

At PND14, retinal degeneration in $Rho^{P23H/+}$ mice was not profound, because the amount of the 11-*cis*-retinal content that equates to the level of Rho was similar to the level found in $Rho^{+/-}$ mice (Table 1). This result was expected, because the amount of P23H opsin constitutes only a small percentage of total Rho as shown previously (20). Here, we used TEM to image the morphology of photoreceptor cell discs of $Rho^{P23H/+}$ and age-matched control mice ($Rho^{+/+}$ and $Rho^{+/-}$) to determine whether abnormal discs are formed before the occurrence of retinal degeneration. Small discs were detected as double membranes or discs in sagittal sections located near the axonemal microtube (AM) in mice of all genetic backgrounds (Fig. 6A–F).

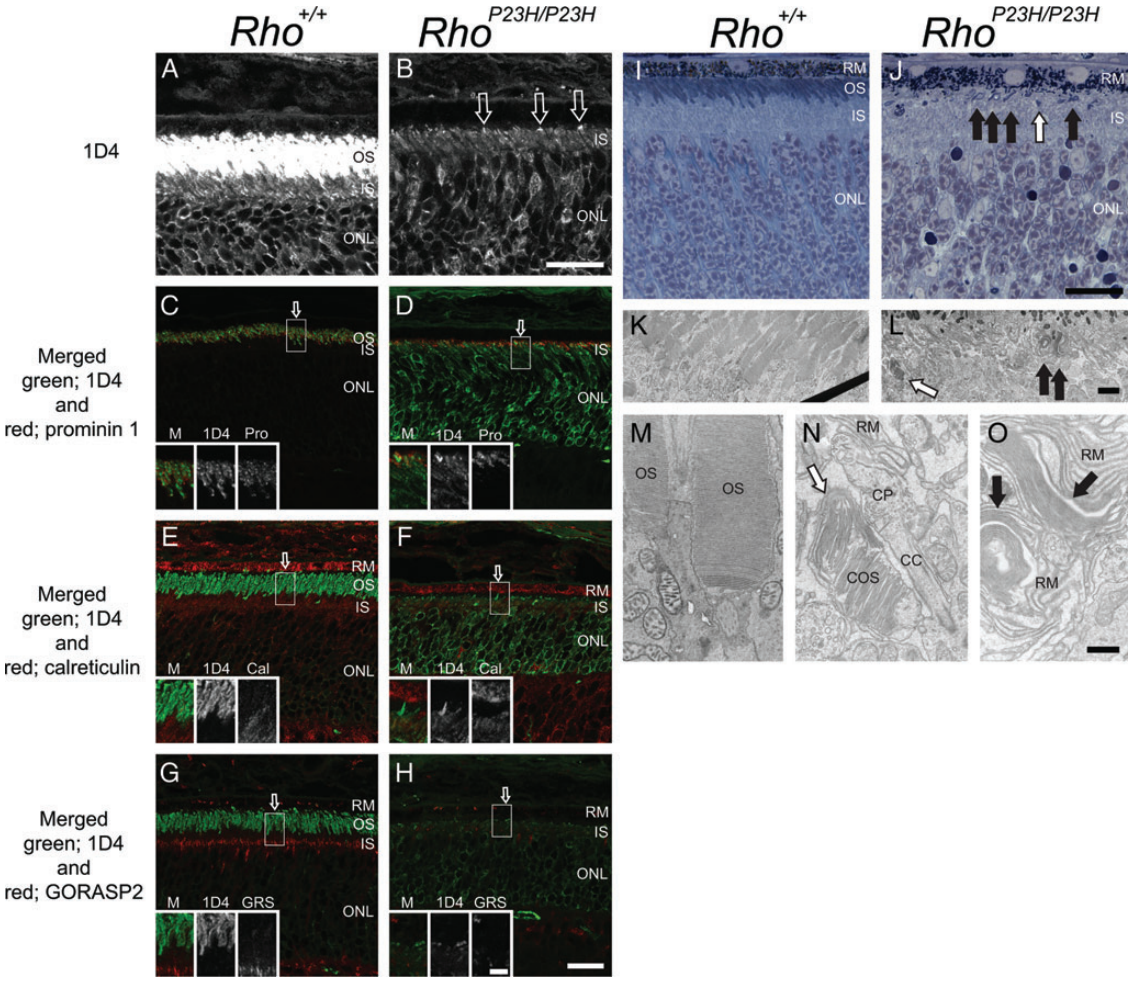

Figure 1. Immunohistochemistry, light microscopy and TEM of *Rho*$^{+/+}$ and *Rho*$^{P23H/P23H}$ mouse retinas suggest elongated disc formation in the *Rho*$^{P23H/P23H}$ mouse retina. *Rho*$^{+/+}$ and *Rho*$^{P23H/P23H}$ mouse retinas at PND14 were analyzed with immunohistochemistry, light microscopy and TEM. Confocal microscopy conditions used to visualize the 1D4 signal in *Rho*$^{P23H/P23H}$ retinas (**B**) resulted in a saturated ROS signal in *Rho*$^{+/+}$ retinas (**A**) with staining also observed in the IS and ONL. 1D4 staining of *Rho*$^{P23H/P23H}$ retinas revealed concentrated needle or dot-shaped structures at the top of the IS (B, arrows) and within the IS layer (B). In *Rho*$^{+/+}$ retinas, opsin and prominin 1 co-localized (**C**, yellow). In *Rho*$^{P23H/P23H}$ retinas, the prominin 1 signal co-localized with the concentrated needle-shaped opsin staining at the top of the IS (**D**, yellow). In *Rho*$^{+/+}$ mouse retinas, opsin (**E**, green) did not co-localize with calreticulin in the IS or RPE (E, red). In *Rho*$^{P23H/P23H}$ mouse retinas, the concentrated needle-shaped opsin structures at the top of IS (F, green) did not co-localize with calreticulin (F, red). In contrast, the needle-shaped structures within the IS layer did co-localize with calreticulin (F, yellow). Opsin (green) did not co-localize with the Golgi reassembly stacking protein 2 (GORASP2) (red) in either *Rho*$^{+/+}$ (**G**) or *Rho*$^{P23H/P23H}$ (**H**) mouse retinas. Higher magnification images of ROS regions indicated by arrows in (C)–(H) are shown in the *insets*. Light microscopy images of toluidine blue stained plastic sections are shown in (**I**) and (**J**). In *Rho*$^{+/+}$ mouse retinas, OS appeared as blue or purple (I, OS). In *Rho*$^{P23H/P23H}$ mouse retinas, in addition to purple colored short OS (J, white arrow), purple colored abnormal OS structures were detected between the IS and RPE (J, black arrows). Thin sections from the same retina shown in (I) and (J) were analyzed by TEM (**K** and **M**, **L**, **N** and **O** for each). In *Rho*$^{+/+}$ mouse retinas, stacks of discs (K and M) were observed. In *Rho*$^{P23H/P23H}$ mouse retina, COS (L and N, white arrows), a CP (N) and packs of elongated discs (L and O, black arrows) are shown. OS, photoreceptor cell outer segment; IS, photoreceptor cell inner segment; ONL, outer nuclear layer; M, merged image; Pro, prominin 1; Cal, calreticulin; GRS, GORASP2; RM, retinal pigment epithelium (microvilli); COS, cone photoreceptor cell outer segment; CP, ciliary protrusion; CC, connecting cilium/cilia. Scale bar: 20 μm (A–J); 5 μm (C–H, *insets*); 2 μm (K and L); 500 nm (M–O).

However, sagittally oriented discs seen in control *Rho*$^{+/+}$ and *Rho*$^{+/-}$ mice were unexpected (Fig. 6A–D). Other than transversely oriented stacks of discs, serial sections of *Rho*$^{+/+}$ mouse retina clearly exhibited single photoreceptor cells containing several sagittally oriented discs at the proximal part of the ROS (Fig. 7). As expected, more developed sagittally oriented abnormal discs were detected before the initiation of rod cell degeneration in *Rho*$^{P23H/+}$ mice (Fig. 6E and F). Thus, it appears that these sagittally positioned discs represent a normal feature of disc formation in young mice, but they become a permanent and more expanded characteristic of the retina in *Rho*$^{P23H/+}$ mice.

To expand these observations, we obtained TEM images of transverse sections of PND14 mouse photoreceptor outer segments (Fig. 8). As in *Rho*$^{+/+}$ mouse retina (Fig. 8B–C), sagittally oriented discs were also detected in *Rho*$^{+/-}$ (Fig. 8D–F) and *Rho*$^{P23H/+}$ (Fig. 8H–I) mouse retinas. Detected sagittally oriented structures clearly represent small discs rather than vesicles or tubular structures (Fig. 6–8). *Rho*$^{+/-}$ and *Rho*$^{P23H/+}$ mice featured an additional one or more transversely aligned

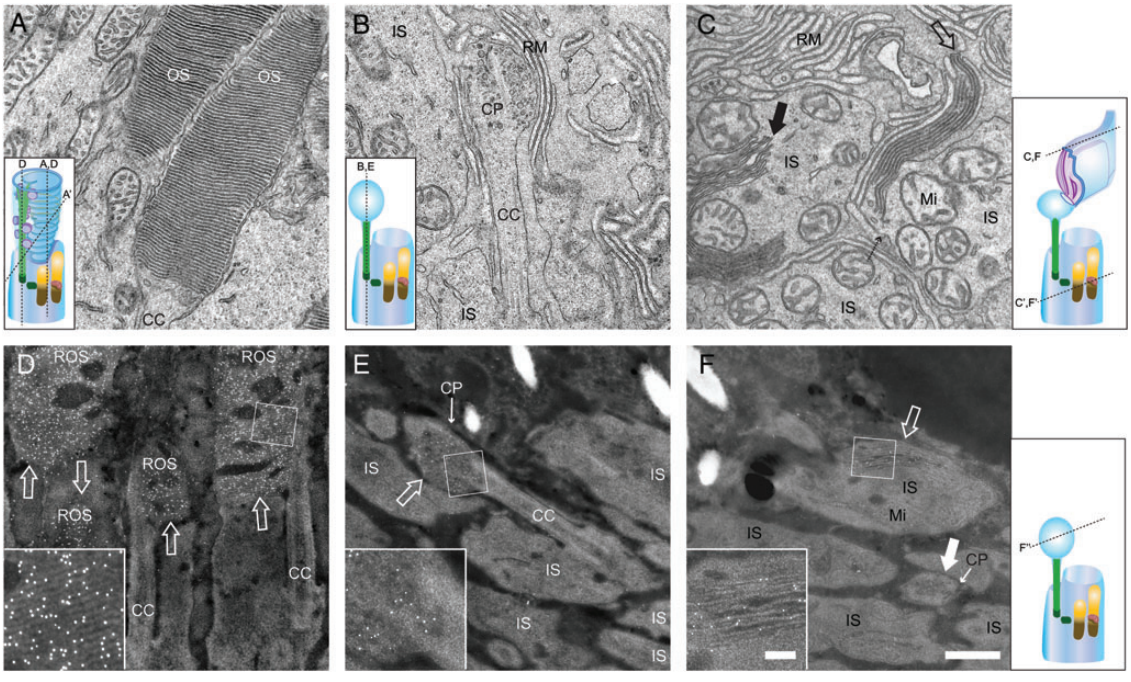

Figure 2. TEM images and immuno-EM labeling of $Rho^{+/+}$ and $Rho^{P23H/P23H}$ mouse retinas reveal transport of P23H opsin to ROS**.** TEM images are shown of photoreceptor cell outer segments (OS) in $Rho^{+/+}$ mice (**A**) and $Rho^{P23H/P23H}$ mice (**B** and **C**). Samples were prepared from PND12 mice. At this PND12, $Rho^{+/+}$ mice exhibited a stack of discs (A). In contrast, $Rho^{P23H/P23H}$ mice featured CPs (B) or packs of elongated discs (C, ⇧) or disc-like structure inside IS (C, ⬆). Note that the plasma membrane between the elongated discs and the IS, indicated by dashed arrow, is not clearly resolved (C), indicating that the plasma membrane around the elongated discs is not continuous with the IS plasma membrane. Immuno-EM images of ROS in $Rho^{+/+}$ (**D**) and $Rho^{P23H/P23H}$ mice (**E** and **F**) at PND12 ($Rho^{+/+}$) and PND12 ($Rho^{P23H/P23H}$). Opsin antibody signals were detected with 5 nm gold particle conjugated secondary antibodies. To enhance membrane structures in immuno-EM samples, scanning transmission electron microscopy (STEM) was used to obtain images. Gold particle signals appearing as white dots were specifically localized in stacks of rod discs in $Rho^{+/+}$ mice (D, ⇧). In contrast, these signals were found in CPs (E, ⇧ and transversely sectioned in F, solid white ⇧) and elongated discs (F, ⇧) in $Rho^{P23H/P23H}$ mice. Higher magnification images (D–F) are shown in the *insets*. OS, photoreceptor cell outer segment; IS, photoreceptor cell inner segment, CP, ciliary protrusion; RM, retinal pigment epithelium microvilli; CC, connecting cilium; Mi, mitochondria; ROS, rod photoreceptor cell outer segment. Hypothetical diagrams of photoreceptor cells are included, indicating the cutting planes with dashed lines. Scale bar: 500 nm (A–F); 100 nm (D–F, *insets*).

small discs around the AM (Fig. 8D–E and G–I). Discs with larger diameters did not exhibit additional transverse discs but instead revealed deep incisures at the AM side (Fig. 8C and F). Traces of three smaller discs occasionally were observed inside (Fig. 8G). Thus, sagittally oriented discs were also present in $Rho^{+/+}$ mice by PND14, but larger amounts of abnormal discs were observed before retinal degeneration occurred in $Rho^{P23H/+}$ mice.

Sagittally oriented discs are still detected in mature rods of $Rho^{P23H/+}$ but not $Rho^{+/+}$ mice

To answer whether sagittally oriented discs are continuously formed after rod cell maturation, we compared transverse sections of $Rho^{+/+}$ and $Rho^{P23H/+}$ mouse retinas at PND63 (Fig. 9). No sagittally oriented discs were observed in $Rho^{+/+}$ retina, suggesting that as discs expand in size vesicles carrying a cargo of Rho easily fuse to form proper discs. However, we did identify sagittally oriented discs in $Rho^{P23H/+}$ mice near the AM, as reported previously (20). This aberrant location is similar to that of discs observed in PND14 mice. Progression of retinal degeneration in $Rho^{P23H/+}$ mice was relatively rapid when rod photoreceptor cells were actively forming new discs (after PND14) and then slowed down a month later when photoreceptor cells had matured. About half of the rod photoreceptor cells in $Rho^{P23/+}$ mice were lost between PND14 and PND40, but no rod photoreceptor cell loss was noted between PND40 and PND63 as measured by 11-*cis*-retinal content that reflects Rho levels (46) (Tables 1 and 2) in agreement with previous histological data (20).

P23H Rho activates the phototransduction cascade

We next investigated whether P23H Rho in these abnormal discs can support phototransduction. Even though P23H Rho has been examined in numerous cell culture and animal models including transgenic *Xenopus*, mouse, pig and rat (9,12,14,22–24,26,28–32,36,37,47), it is still not clear whether P23H Rho can activate rod phototransduction and, if so, how its signaling compares to that of Rho itself. $Rho^{P23H/P23H}$ mice allowed us to address this question. We initially attempted to perform single-cell suction recordings from rods of 2-week-old $Rho^{P23H/P23H}$ mice but failed to identify ROS even at the retinal edge because of severe ROS degeneration. Thus, we performed transretinal ERG recordings instead to obtain photoresponses across the whole retina from $Rho^{+/+}$, $Rho^{P23H/+}$ and $Rho^{P23H/P23H}$ mice. All mice studied were only 14–16 days old to minimize the effects of severe photoreceptor degeneration in $Rho^{P23H/P23H}$

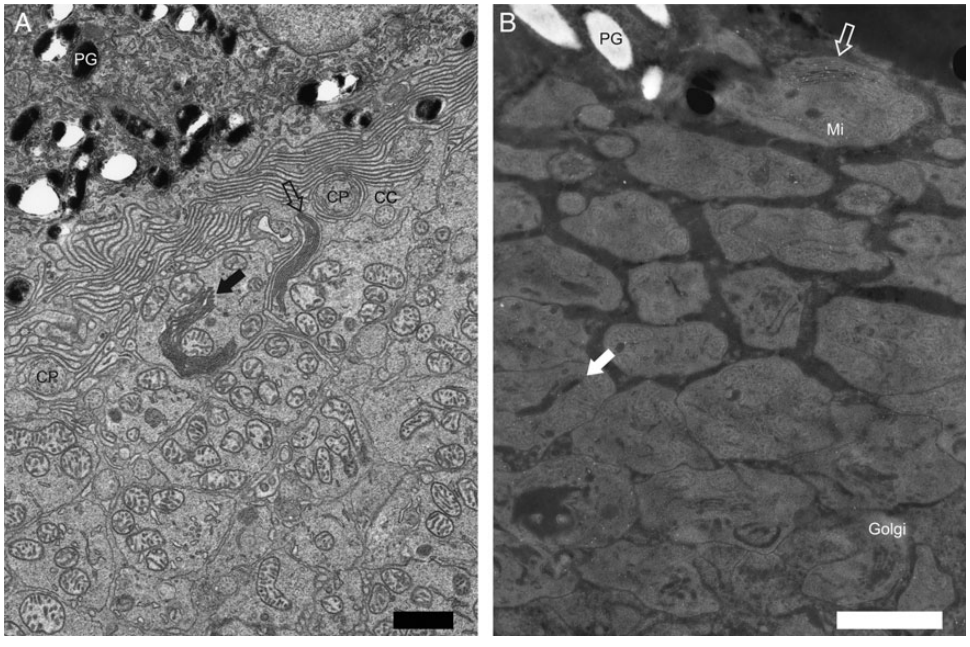

Figure 3. Low magnification images of Figure 2C and F. Low magnification images of Figure 2C (**A**) and Figure 2F (**B**). *Rho*$^{P23H/P23H}$ mice featured elongated discs (A and B, ⇧) or disc-like structures inside the IS (A and B, ⬆ and solid white ⇧). In contrast to elongated discs (A, ⇧), disc-like structures inside the IS were located near the center of the IS (A, ⬆). Opsin was predominantly located at the elongated discs (B, ⇧), which were adjacent to the IS and retinal pigment epithelium. Less intense opsin staining was also detected at disc-like structures inside the IS (B, solid white ⇧). Black spaces within IS disc-like structures (B, solid white ⇧) likely correspond to empty space, an artifact of immuno-EM sample preparation. In the *Rho*$^{+/+}$ mouse immuno-EM samples, a similar artifact was often observed between discs (Fig. 2D). PG, pigment granule of the RPE; Golgi, Golgi apparatus. Other abbreviations are the same as in Figure 2. Scale bar: 1 μm.

retinas (20). Transretinal ERG recordings were done with synaptic inhibitors to block post-photoreceptor components of the photoresponse and isolate pure rod- and/or cone-driven ERG a-waves (see Materials and Methods for details). Figure 10 shows typical test-flash response families for *Rho*$^{+/+}$ (Fig. 10A), *Rho*$^{P23H/+}$ (Fig. 10B) and *Rho*$^{P23H/P23H}$ (Fig. 10C) retinas. *Rho*$^{P23H/+}$ retinas produced robust rod responses but with slightly reduced (by 5%) maximal response amplitudes. Based on the increase in half-saturating light intensity ($I_{1/2}$) measured from the corresponding intensity–response curves (Fig. 11A), the photosensitivity of rods in *Rho*$^{P23H/+}$ retinas was reduced by 1.6-fold, consistent with the reduction in 11-*cis*-retinal in *Rho*$^{P23H/+}$ retinas (Table 1). In contrast, responses from *Rho*$^{P23H/P23H}$ retinas demonstrated dramatically reduced (by 5.7-fold) amplitudes and their sensitivity was, on average, 44-fold lower than that of control retinas. Thus, severe ROS degeneration of the *Rho*$^{P23H/P23H}$ mouse retina dramatically reduced the overall amplitude and sensitivity of light responses from its photoreceptors.

Because 11-*cis*-retinal could help in stabilizing P23H opsin (11,20,22), we tested whether the lower response of *Rho*$^{P23H/P23H}$ rods resulted from possible retinoid deficiency under normal dark-adapted conditions. However, acute treatment of *Rho*$^{P23H/P23H}$ retinas with 130 μM exogenous 11-*cis*-retinal (at room temperature for 1 h and in the presence of 1% bovine serum albumin) did not increase their light sensitivity response (Fig. 11A). In previous control experiments, such treatment with 11-*cis*-retinal completely restored rod sensitivity in chromophore-deficient retinas from RPE65 knockout mice (48). This result suggests that inefficient signaling in *Rho*$^{P23H/P23H}$ retinas did not result from retinoid deficiency.

Typically in mouse retina, rods are more sensitive and produce substantially larger responses than cones (49). However, in *Rho*$^{P23H/P23H}$ mouse retinas, the amplitude and sensitivity of the overall transretinal ERG responses were comparable with those of cones, making it difficult to separate the response component produced by *Rho*$^{P23H/P23H}$ rods from that of cones. To resolve this issue, we performed recordings from *Rho*$^{P23H/P23H}$ mice either lacking the rod G protein transducin (*Gnat1*$^{-/-}$ mice) essential for rod phototransduction or lacking the functional cone-specific G protein (*Gnat2*$^{cpfl3/cpfl3}$ mice) needed to activate the cone signaling pathway. Therefore, *Rho*$^{P23H/P23H}$ mice with *Gnat1*$^{-/-}$ or *Gnat2*$^{cpfl3/cpfl3}$ backgrounds (*Gnat1*$^{-/-}$*Rho*$^{P23H/P23H}$ and *Gnat2*$^{cpfl3/cpfl3}$Rho$^{P23H/P23H}$) allowed us specifically to examine the rod and cone components of transretinal responses from *Rho*$^{P23H/P23H}$ retinas. As expected, the cone-driven responses from *Gnat1*$^{-/-}$*Rho*$^{P23H/P23H}$ retinas (Fig. 10D) were smaller, faster and 35-fold less sensitive than the rod-driven responses of control *Rho*$^{+/+}$ retinas (Fig. 10A). Notably, the *Gnat2*$^{cpfl3/cpfl3}$Rho$^{P23H/P23H}$ retinas lacking functional cones also produced detectable responses which directly demonstrate that P23H Rho in *Rho*$^{P23H/P23H}$ rods can be activated by light and generate a photoresponse. However, the rods in *Gnat2*$^{cpfl3/cpfl3}$ Rho$^{P23H/P23H}$ mice were extremely desensitized (~17 000-fold) as compared with rods in *Rho*$^{+/+}$ animals. As a consequence, rods in the *Rho*$^{P23H/P23H}$ retina, rods were ~500-fold less sensitive than cones (Fig. 11B). The maximal response amplitude from rods in *Gnat2*$^{cpfl3/cpfl3}$Rho$^{P23H/P23H}$ mice was also lower than that from cones in *Gnat1*$^{-/-}$*Rho*$^{P23H/P23H}$ retinas. As a result, the overall flash responses from *Rho*$^{P23H/P23H}$ retinas were dominated by cones.

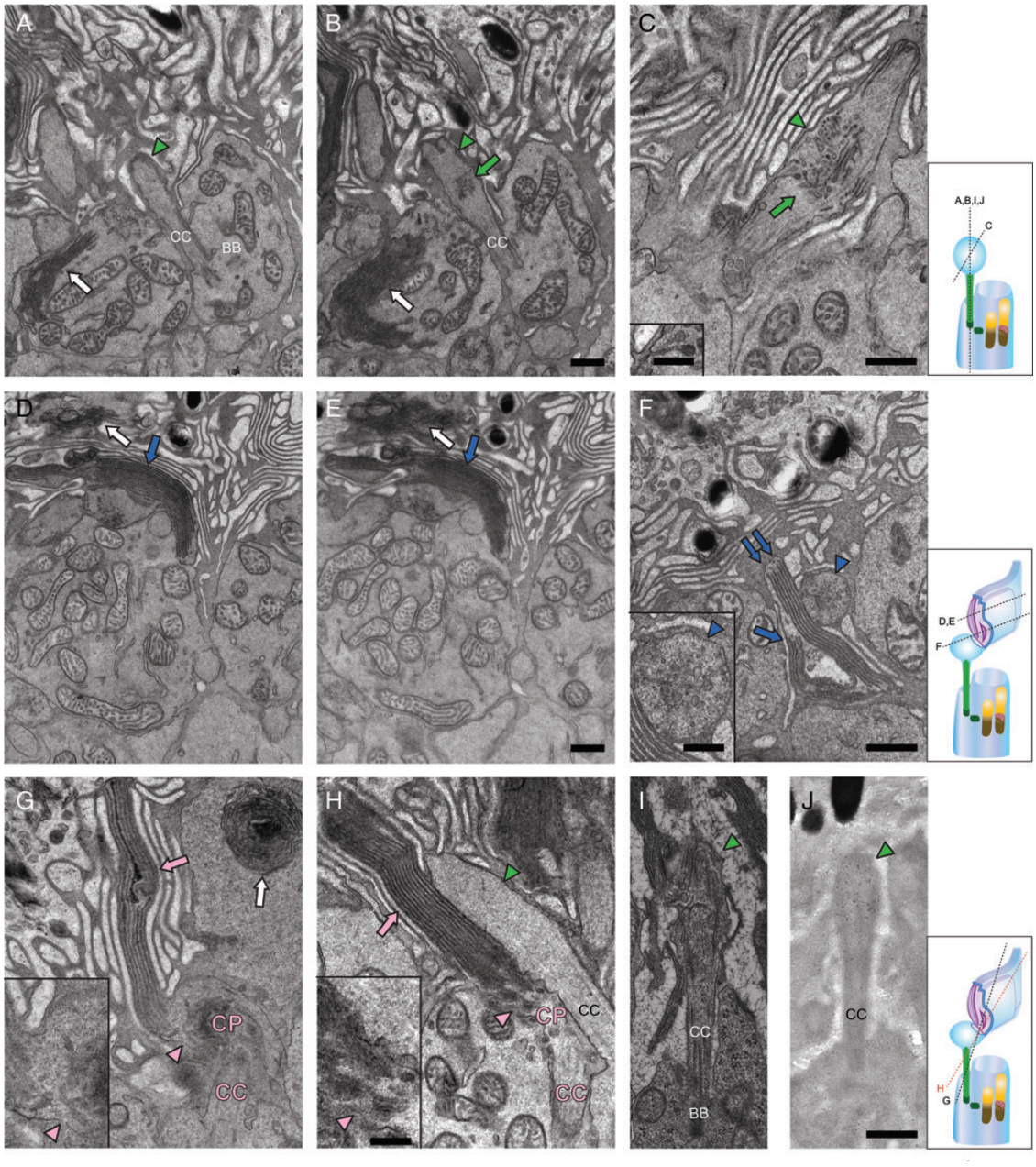

Figure 4. TEM images of serial sections from *Rho*$^{P23H/P23H}$ mouse retinas reveal elongated discs. TEM images of rod photoreceptor cell outer segments (OS) in *Rho*$^{P23H/P23H}$ mice at PND12 (**A**–**H**) and at PND14 (**I** and **J**). (A) and (B) show serial sections 1 and 5 through the same CP, whereas (C) shows another CP. The green triangles indicate CPs and the green arrows point to tubules and vesicles observed in the internal space of CPs. Tubules and vesicles were not seen in the internal space of CC. Endocytosis of the CP plasma membrane with a deep invagination, called a 'neck' is apparent in C (*inset*), indicating that tubules and vesicles are formed by endocytosis of the CP plasma membrane. White arrows point to disc-like structures inside the IS. Different from elongated discs, such structures were dramatically changed in the serial sections. (D)–(E) show serial sections 1 and 5 through the same elongated disc. Blue arrows point to elongated discs that were continuously detected in all five serial sections covering a total thickness of about 400 nm (5 × 80 nm) and suggesting that these are elongated discs rather than tubules. White arrows point to disc-like structures inside the IS. Although CCs were observed in photoreceptor sagittal sections, elongated discs were mainly detected as isolated structures in transverse sectional views, either adjoining inner segments or surrounded by microvilli of RPE cells (D–F). The CP adjoining these elongated discs, seen in transverse orientation, is indicated with blue triangles (F, *inset*). The typical number of elongated discs per photoreceptor cell was 9–11. In some cases, they formed two branches, one containing six discs (F, blue double arrow) and the other four discs (F, blue single arrow). Rarely, elongated discs (pink arrows) were seen connected to a CP in sagittal sections (G–H). But even in such cases, the CC (labeled in pink) appeared in a transverse sectional orientation, suggesting a skewed orientation of that photoreceptor with respect to the plane of the section. Note that CPs adjoining such elongated discs appeared as sagittally-cut structures (H, green triangle), indicating that elongated discs had to be laterally connected to a CP. Also, CPs connected to elongated discs did not show clear tubular or vesicular structures (G and H, pink triangles), in contrast to CPs which were not connected to elongated discs (B and C, green arrows and F, *inset*, blue triangle). The last observation indicates that tubules and vesicles are cleared by fusion to elongating discs. White arrows point to disc-like structures inside the cell (G). CPs were also detected at PND14 (I and J, green triangle). Similar to PND12, two opsin antibodies (4D2 and 1D4) specifically labeled CPs (J, green triangle and data not shown). BB, basal body; CC, connecting cilium/cilia. Other abbreviations are the same as in Figure 2. Hypothetical diagram of photoreceptor cells within cutting planes is indicated by dashed lines. Scale bar: 500 nm (A–J); 200 nm (C, F, G and H, *inset*).

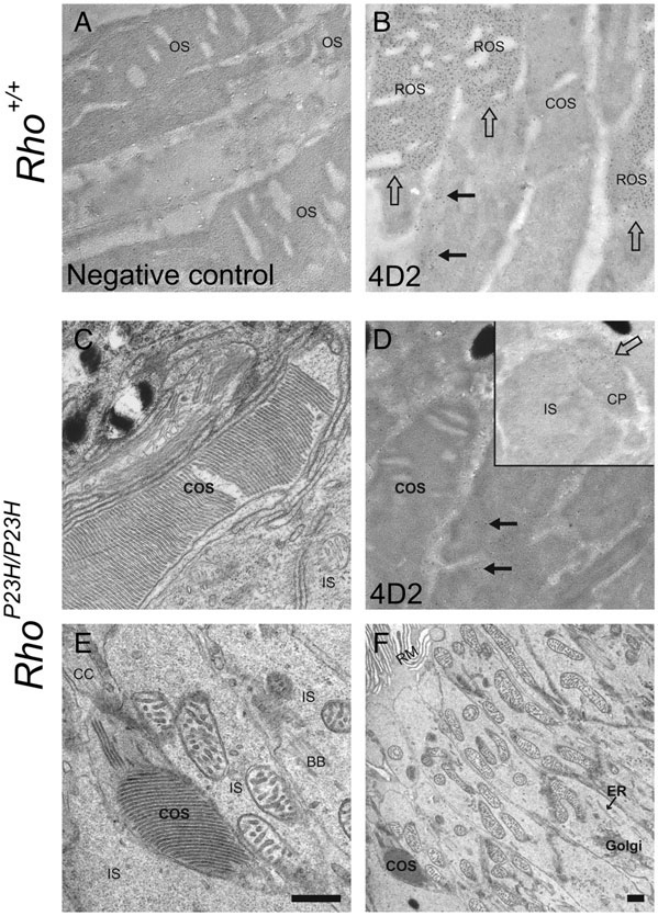

Figure 5. TEM and immuno-EM images of $Rho^{+/+}$ and $Rho^{P23H/P23H}$ mouse cone cells. Retinal TEM images of immuno-EM samples prepared from PND14 $Rho^{+/+}$ and $Rho^{P23H/P23H}$ mice are shown (**A**–**D**). No immunostaining was detected in the $Rho^{+/+}$ negative control (A). (B) In $Rho^{+/+}$ mouse retina, opsin antibody (4D2) specifically labeled ROS (B, ⇧) but not cone outer segments (COS). (C) In the $Rho^{P23H/P23H}$ mouse retina, only COS exhibited a normal stack of discs. COS were not labeled with opsin antibody (4D2) (D). In contrast, CP in the same grid were labeled with opsin antibody (D, *inset*, ⇧). A fine opsin signal was detected in rod photoreceptor cell inner segments (B and D, ←) in both $Rho^{+/+}$ and $Rho^{P23H/P23H}$ mouse retinas. At PND12, $Rho^{P23H/P23H}$ mice exhibited a low prevalence of COS (**E**) relative to PND14 (C) and these COS were often located between inner segments and not attached to RPE microvilli (**F**). (E) presents a higher magnification of the COS image shown in (F). BB, basal body; ROS, rod photoreceptor cell outer segment; COS, cone outer segment; ER, endoplasmic reticulum;Golgi, Golgi apparatus. Other abbreviations are the same as in Figure 2. Scale bar: 500 nm.

Phototransduction in photoreceptors expressing P23H opsin

Rod-driven responses in $Gnat2^{cpfl3/cpfl3}Rho^{P23H/P23H}$ retinas allowed us to characterize phototransduction activation and inactivation in P23H mutant rods. To evaluate how the P23H mutation of opsin affects its ability to activate rod phototransduction, we compared the rising phases of averaged (cell population mean) dim flash responses from the four P23H and one control mouse lines normalized to the maximal response amplitude (dark voltage) for each retina (Fig. 11C). These responses corresponded to light intensities at which their amplitudes were ∼0.25–0.35 of maximal amplitude and fell into the linear range of the intensity–response relationship. The test flash light intensity was 14 photons μm^{-2} in the case of $Rho^{+/+}$ and $Rho^{P23H/+}$ retinas, 392 photons μm^{-2} for the $Rho^{P23H/P23H}$ and $Gnat1^{-/-}Rho^{P23H/P23H}$ retinas and 1.1×10^4 photons μm^{-2} for $Gnat2^{cpfl3/cpfl3}Rho^{P23H/P23H}$ retinas. Averaged responses of mutant cells were then individually scaled down to make their activation (rising) phase coincide with that of the $Rho^{+/+}$ response. Thus, amplification of the phototransduction cascade was reduced, on average, by (392/13.9)/8 (scaling factor) = 3.5-fold in both $Rho^{P23H/P23H}$ and $Gnat1^{-/-}Rho^{P23H/P23H}$ photoreceptors, clearly placing it in the cone range. In addition, photo-responses in these two mouse lines were substantially faster than those in $Rho^{+/+}$ rods (Fig. 11C), again indicating that cones dominated light detection in $Rho^{P23H/P23H}$ mouse retinas. As mentioned above, $Gnat2^{cpfl3/cpfl3}Rho^{P23H/P23H}$ rods were dramatically desensitized and their phototransduction amplification declined by ∼800-fold compared with that in control rods. Rod responses from $Gnat2^{cpfl3/cpfl3}Rho^{P23H/P23H}$ retinas were substantially faster than in control rods, although still slower than cone responses recorded from $Gnat1^{-/-}Rho^{P23H/P23H}$ retinas or the cone-dominated responses from $Rho^{P23H/P23H}$ retinas (Fig. 11D). Finally, heterozygous $Rho^{P23H/+}$ retinas displayed intermediate photoresponse kinetics. Together, these results demonstrate that in addition to dramatically reducing the amplification of phototransduction, P23H Rho produced a substantial acceleration in the shutoff of phototransduction in these desensitized rods.

Table 1. Amounts of 11-cis-retinal at PND14 in $Rho^{+/+}$, $Rho^{+/-}$ and $Rho^{P23H/+}$ mice[a]

Mice	11-*cis*-retinal (pmol/eye)	*n* (total eyes)
$Rho^{+/+}$	171 ± 25.1	4 (14)
$Rho^{+/-}$	89.5 ± 13.9	5 (26)
$Rho^{P23H/+}$	89.8 ± 7.6	3 (16)

[a]Amounts of 11-*cis*-retinal in dark adapted eyes were analyzed by normal phase high-performance liquid chromatography (HPLC). There was no significant difference in 11-*cis*-retinal content between $Rho^{+/-}$ and $Rho^{P23H/+}$ mice at PND14. Consistent with the single $Rho^{+/+}$ allele, the amount of 11-*cis*-retinal in $Rho^{+/-}$ *and* $Rho^{P23H/+}$ mice was about half of that in $Rho^{+/+}$ mice. Values are means ± SD. *n*, number of repeated analyses.

Retinal degeneration in $Rho^{P23H/+}$ mice is not caused by aberrant signaling

The ERG responses of $Rho^{P23H/P23H}$ mice imply that P23H opsin is transported to the ROS. One possibility is that aberrant phototransduction mediated by transducin is the real cause of retinal degeneration. Thus by carrying out a quantitative analysis of retinal degeneration in mice lacking the rod G protein transducin ($Gnat1^{-/-}$ mice), we found that P23H Rho-mediated phototransduction was not a major cause of retinal degeneration in $Rho^{P23H/+}$ mice. We found that in 4 out of 16 regions, there was significant drop of photoreceptor nuclei in $Gnat1^{+/+}$ $Rho^{P23H/+}$ mouse, compared with $Gnat1^{-/-}Rho^{P23H/+}$ mouse. However, retinal degeneration progressed even though rod cell signal transduction was blocked in *Gnat1* knock-out mice ($Gnat1^{-/-}Rho^{P23H/+}$) (Fig. 12), a finding consistent with the smaller amount of P23H opsin found in $Rho^{P23H/+}$ mice.

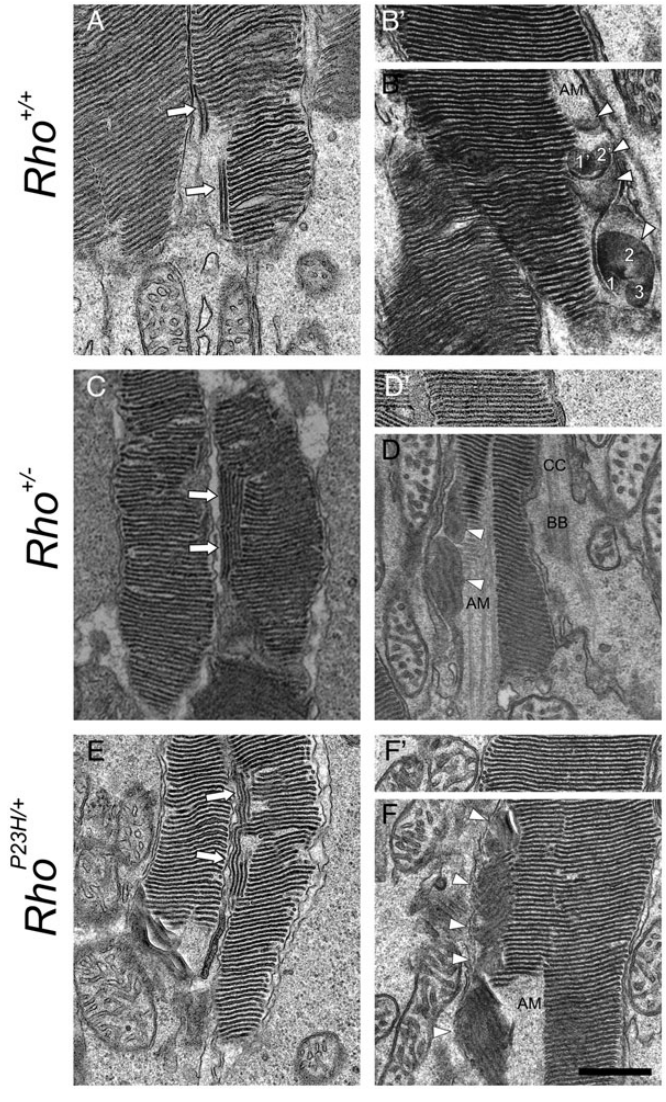

Figure 6. Retinal TEM images of sagittal sections of PND14 mouse photoreceptor cell outer segments demonstrate sagittally oriented small discs adjoining normal stacks of discs. Sagittally oriented small discs were detected as double membranes (⇧) or discs (Δ) in photoreceptor sagittal sections (**A**–**F**). Those discs were next to stacks of normally oriented discs (A, C and D), the AM and stocks of normally oriented discs (B, D and F). (B), (D) and (F) show transverse sectional views of sagittally oriented small discs located close to proximal ends of outer segments. Note that two sagittally oriented small discs in (B) exhibit a trace of two (1′, 2′) or three smaller discs (1,2,3) with (B′), (D′) and (F′) showing distal parts of same outer segment. At the distal ROS, these discs are enlarged but normally oriented. CC, connecting cilium; AM, axonemal microtube; BB, basal body. Scale bar: 500 nm.

DISCUSSION

Here, we first questioned whether the P23H opsin could cause formation of partially disorganized sagittal discs in rod photoreceptor cells. Mutations or lack of disc morphogenic proteins can cause progressive retinal degeneration (42,43) with the common feature of disorganized sagittally oriented discs. Indeed, such structures have already been observed in a mouse model of adRP caused by the P23H opsin ($Rho^{P23H/+}$) (20). But because rod opsin antibody recognizes both P23H opsin and Rho, it was unclear whether the P23H opsin produced this phenotype. In this study, we found that $Rho^{P23H/P23H}$ mice formed CPs and occasional immature sagittally aligned elongated discs at PND12 (Figs 2B and C, 3A and B, 4). Because $Rho^{-/-}$ mice cannot form rod discs (4,5), this indicates that the elongated sagittal discs were formed by P23H opsin. Although P23H opsin is endoglycosidase H sensitive (20), we found P23H opsin surprisingly was predominantly transported to CPs or elongated discs. Why does EndoH-sensitive P23H opsin travel to the ROS? Such a pathway is still not fully characterized in photoreceptor cells. But trafficking of TRPP2 (polycystic kidney disease 2-like 1 protein also known as transient receptor potential polycystic 3) (50) to ciliary plasma membrane via a non-conventional pathway in cultured cells and TRP channel to COS of the mouse retina (51) suggest that non-conventional pathways also exist in rod photoreceptor cells.

Typical numbers of elongated discs surrounded by a plasma membrane were 6 or 9–11. Occasionally, there was a space between the six and additional four discs (Fig. 4F). Typical diameters of elongated discs were 1.1, 1.5 and 1.9 μm (measured by rim to rim length in sagittal sections), which were larger than that of cone discs at the same age (0.92 μm) (Fig. 5E and F), a finding also consistent with elongated disc formation by P23H opsin. Three reasons could explain why $Rho^{P23H/P23H}$ mice do not elaborate normal ROS disc structures. One is that P23H opsin itself cannot form properly aligned disc structures, and another is that the extremely low amounts of opsin cannot form properly aligned disc structures. Finally, and perhaps the most likely explanation for the lack of normal ROS formation is a combination of both the above effects. CPs have long been noted in $Rho^{+/+}$ mice at an early developmental stage with Rho specifically localized in these structures (52). Un-oriented primitive rod sacs have been reported in PND8 and PND12 white mice (53,54). Elongated disc-like structures also have been noted at PND8 in rat retina (55). Thus, rods expressing P23H opsin probably demonstrate an early step in disc formation because they fail to form organized mature discs. The absence of vesicles at the CC supports the contention that vesicles and tubules are not transported from rod inner segments but instead could be formed by endocytosis of plasma membrane at the CPs (Fig. 4C). Interestingly, not all vesicles expressed P23H opsin (Fig. 2E), consistent with such a mechanism for vesicle formation. The prevalence of CPs was greater than that of elongated discs, although the elongated discs were larger than the CPs, indicating that many rod cells either did not form discs or were phagocytized by the RPE. The decrease of packs of elongated disc structures but not CPs observed in PND14 TEM images of $Rho^{P23H/P23H}$ mice supports an active phagocytosis of discs expressing P23H opsin (Figs 1L, N, and O, 4I and data not shown).

Connections of CCs with elongated discs were barely detectable in TEM images of thin (∼80 nm) sections, although these structures were readily observed in normal mouse retina. There are at least four possible explanations for this observation. One is that there are no connections between elongated discs and CCs, so both structures cannot exist in one section. A second possibility is that elongated discs detach from a CC shortly after they are formed. The third scenario is that elongated discs could form at the inner segment and not the distal end of a CC. The fourth possibility is that elongated discs are laterally connected to CPs, i.e. the orientation of the elongated discs is skewed with

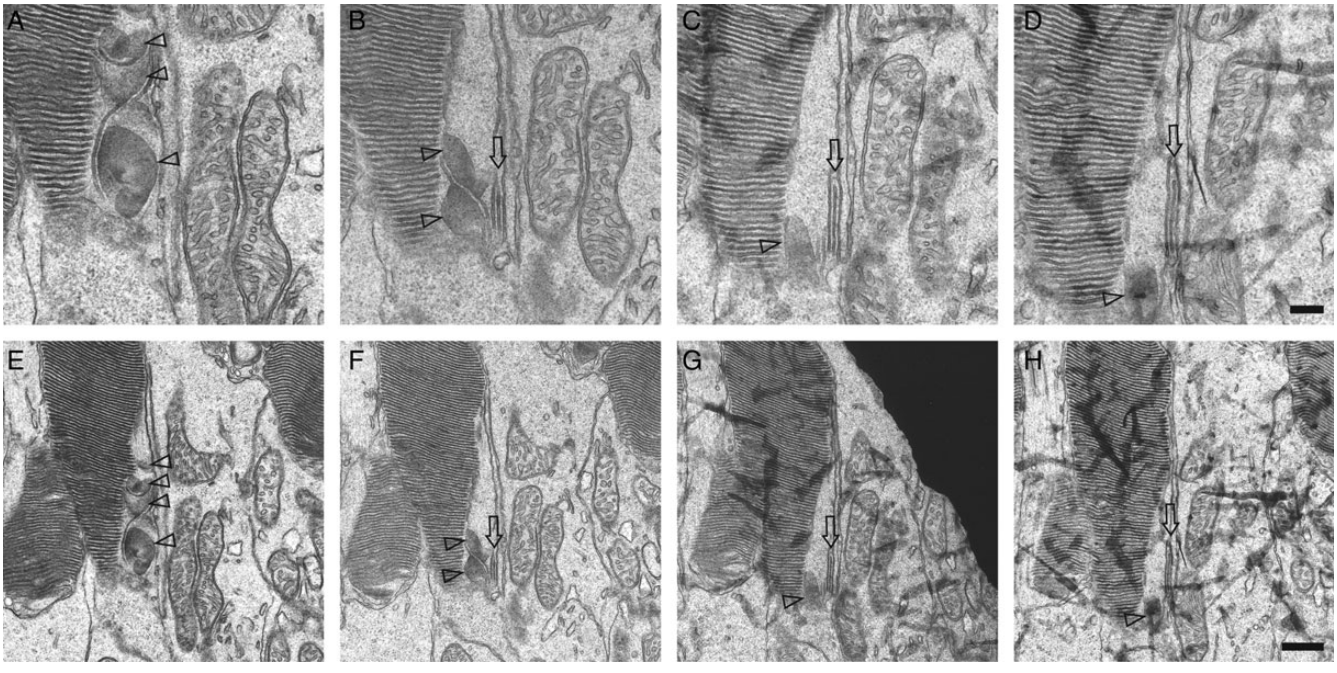

Figure 7. Retinal TEM images of serial sections from $Rho^{+/+}$ mouse retinas reveal a series of sagittally oriented discs. TEM images are shown of four serial sections prepared from $Rho^{+/+}$ mice at PND14 (**A**–**D**). These covered a thickness of ∼320 nm of photoreceptor cells or ∼80 nm for each section. (**E**–**H**) Lower magnification images of (A)–(D). Note that small sagittally aligned disc(s) are shown in four of four serial sections at the proximal part of the same photoreceptor cell (Δ). Also, sagittally oriented three double membranes (⇧) are present in three of the four serial sections. Scale bar: 200 nm (A–D) and 500 nm (E–H).

respect to the CC. Thus, the ∼80 nm thickness of sagittal sections through a CC contains the CP but cannot show laterally connected elongated discs.

In $Rho^{P23H/+}$ mice, we found sagittally oriented discs that formed prior to retinal degeneration at PND14 (Figs 6E and F, 8H and I). Interestingly, at PND63, after the loss of half of the rod cells, sagittally oriented discs were still localized near the axonemal microtubule in the proximal ROS, the site of daily disc formation (Fig. 9D–F). Collectively, these observations suggest that sagittally oriented elongated discs seen in $Rho^{P23H/+}$ mice are caused by abnormal disc formation rather than disorganization of normal discs. Our observations do not address the possibility that different factors could affect sagittal-disc formation in young and older mice but evidence for such modifying factors has yet to be documented.

The impact of sagittally aligned discs on retinal degeneration is still unclear. $Rho^{P23H/+}$ mice exhibited relatively rapid retinal degeneration in first month of life (they lost 50% of rod cells between PND14 and PND40, Tables 1 and 2) and slow retinal degeneration thereafter (no loss of rod cells between PND40 and PND63, Table 2). Rod photoreceptor cells expressed nearly complete outer segment components by PND12–16 which matured into ROS by 1 month of age. During maturation (between PND12 and PND30), the number of discs per cell increased and then remained stable. Thus, the rate of retinal degeneration in $Rho^{P23H/+}$ mice after PND14 correlated with the rate of disc formation. It is already known that mis-oriented discs can also be formed by mutations in proteins considered important for disc morphogenesis that produce retinal degeneration (42,43,44,56). But rates of retinal degeneration in such mouse models differ. Accordingly, a 50% loss of photoreceptors occurred by 7 weeks in R373C prominin 1 mutant transgenic mice (43), two to three rows of ONL nuclei were lost by PND30 in RP1 mutant homozygote mice (44) and a normal thickness of ONL at PND30 but a complete loss of rod photoreceptor cells by 3–4 months of age was noted in Cngb1 knockout mice (42). Thus, sagittally aligned disc formation could have some impact on retinal degeneration. In addition to such structural abnormalities, excess phagocytosis could also have contributed to retinal degeneration. In $Rho^{P23H/P23H}$ mice, a decrease of packs of elongated disc structures but not CPs was observed in PND14 mice. In $Rho^{P23H/+}$ mice, it is reasonable to consider that sagittally oriented discs contain P23H opsin. Although it is still unclear whether these disks consist of P23H opsin alone or together with WT opsin, morphological disorganization plus the existence of P23H opsin in abnormal discs may facilitate phagocytosis not only of P23H opsin-containing discs but also WT opsin-containing discs. More information is required to answer this question. The above observations in P23H opsin mice stimulated us to investigate disc morphogenesis in normal mice. Surprisingly, we also found sagittally oriented discs in $Rho^{+/+}$ retina at PND14. Our serial transverse and sections analyses strongly indicate that such discs appear at the proximal OS where new discs are actively formed. Immature discs with un-oriented or random alignments were reported in PND8 and PND12 $Rho^{+/+}$ BALB/c and white mice (40,53), but detail information on un-oriented discs had been unknown (53). We found that sagittally oriented discs in PND14 $Rho^{+/+}$ B6 mice were ordered and located in the space between normal discs and the plasma membrane. These discs were small and sometimes consisted of fusions of even smaller discs. Thus, we hypothesize that disc maturation involves initial formation of sagittally oriented small discs that probably change their angles

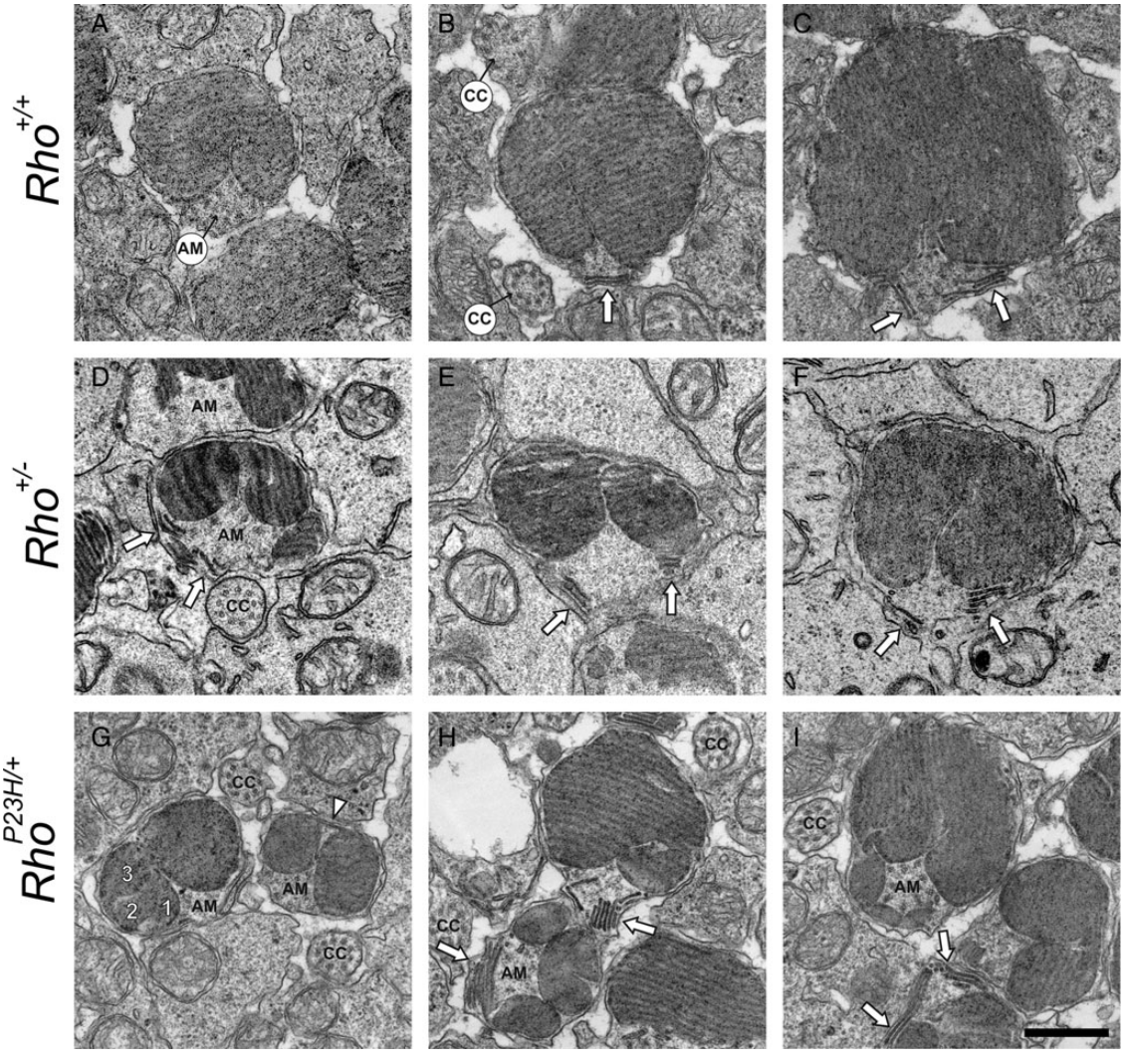

Figure 8. TEM images of transverse sections of PND14 mouse photoreceptor cell outer segments demonstrate sagittally oriented small discs near the AM. Retinal samples were prepared from $Rho^{+/+}$ (**A**–**C**), $Rho^{+/-}$ (**D**–**F**) and $Rho^{P23H/+}$ (**G**–**I**) mice at PND14 and proximal photoreceptor cell outer segments were imaged. In transverse sections, discs exhibited a typical moiré pattern. In addition to such normal discs, several sagittally aligned small discs were located near the AM in $Rho^{+/+}$, $Rho^{+/-}$ and $Rho^{P23H/+}$ mice (⇧). Moreover, $Rho^{+/-}$ and $Rho^{P23H/+}$ mice exhibited an additional one or more transversely aligned small discs around the AM (D–E, G–I). $Rho^{+/+}$ mice did not display additional transverse discs but instead revealed deep incisures at the AM side (A and B). Note that one small disc in image G exhibited traces of three smaller discs inside (1,2,3). Δ, an electron-dense linear structure bridged two small discs (G). Abbreviations are as in Figure 6. Scale bar: 500 nm.

and fuse to transversely oriented discs to create mature discs at the proximal ROS.

Sagittally oriented discs at the distal ends of cone cells in adult $Rho^{+/+}$ retina have been reported (57). For several decades, mature rod cells of greater than 1-month-old $Rho^{+/+}$ mice have been analyzed by TEM. However, to our best knowledge, sagittally oriented discs in healthy mature rod photoreceptor cells have not been reported. Two possible explanations come to mind. One is that sagittally oriented disc formation is temporal in immature rod cells, and thus not observed in mature rod photoreceptors. The other possibility is that sagittally oriented discs are formed in mature rod cells, but change to a transverse orientation so rapidly as to become virtually undetectable. Because the thickness of a single disc is ∼21 nm and the diameter of a mature stack of discs is ∼1.27 μm (58,59), a sagittal thin section (∼80 nm) could reveal many transversely oriented discs, but possibly miss those few with a sagittal orientation. After maturation of photoreceptor cells in mice, new disc formation is expected to decrease as compared with PND14 retina. Indeed, we did not detect sagittally oriented discs at the AM side in $Rho^{+/+}$ mice at PND63. However, we did find sagittally oriented discs in PND63 $Rho^{P23H/+}$ mice located near the AM. This suggests that the formation of sagittally oriented abnormal discs in $Rho^{P23H/+}$ mice is continuous and that the problem lies with their failure to align transversely. More than two discs connected transversely to each other in $Rho^{+/-}$ and $Rho^{P23H/+}$ mice (Fig. 8D, E and G–I) contained half the normal amount of Rho (Table 1). Moreover, at least one of these brother discs showed the same location of incisures as $Rho^{+/+}$ photoreceptor cells possessing the full complement of opsin. Possibly, this divided disc

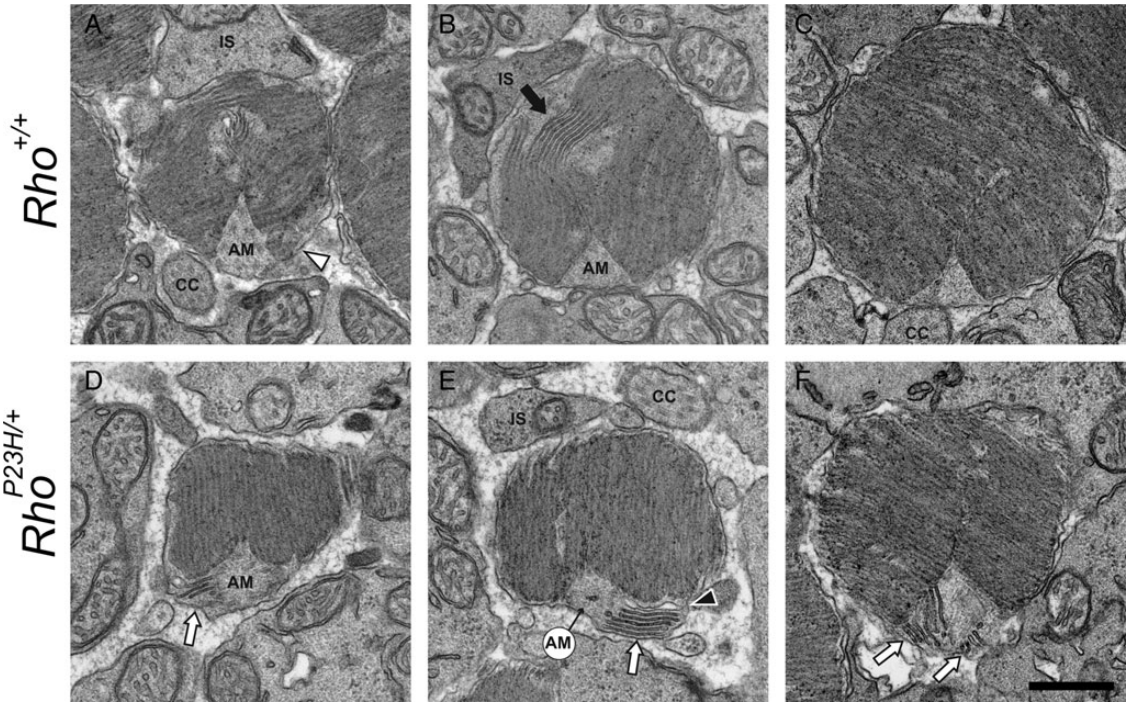

Figure 9. TEM images of transverse sections of PND63 mouse photoreceptor cell outer segments reveal sagittally oriented discs near the axonemal microtube (AM) in $Rho^{P23H/+}$ mice but not in $Rho^{+/+}$ mice. At PND63, mature photoreceptor cells continuously synthesize new discs at the proximal outer segment where the opposite side of the AM is surrounded by the distal inner segment (A, IS). In $Rho^{+/+}$ mice at PND63, sagittally aligned discs were not seen around the AM (**A**–**C**), but transversely aligned small discs were detected instead (A, Δ). Also, a different type of sagittally aligned disc was located at the side opposite the AM (B, ⬆). Routinely observed, this type of disc did not display a rim and both ends of it were connected to transversely aligned discs, indicating that these sagittally aligned discs represented partially folded transversely aligned discs at the proximal part of the ROS. In $Rho^{P23H/+}$ mice, sagittally aligned discs were still seen around the AM (**D**–**F**, ⇧). The open disc indicated by a black arrowhead in (E) was probably an artifact caused by sample preparation. Similar types of open discs were also noted in the ROS of $Rho^{+/+}$ mouse retinas (data not shown). Abbreviations are as in Figure 6. Scale bar: 500 nm.

Table 2. Amounts of 11-*cis*-retinal and Rho at PND40 and PND63 in $Rho^{+/+}$ and $Rho^{P23H/+}$ mice[a]

Mice	PND40 ± 3	*n* (total eyes)	PND63 ± 3	*n* (total eyes)	*P*-value
11-*cis*-retinal (pmol/eye)					
$Rho^{+/+}$	602 ± 65.1	4 (16)	665 ± 143	4 (14)	0.44
$Rho^{P23H/+}$	165 ± 24.2	4 (16)	172 ± 35.1	3 (12)	0.77
Rhodopsin (Rho) (pmol/eye)					
$Rho^{+/+}$	860 ± 66.9	7 (19)	928 ± 128	3 (23)	0.29
$Rho^{P23H/+}$	204 ± 31.0	7 (51)	198 ± 22.8	3 (17)	0.75

[a]Amounts of 11-*cis*-retinal in dark adapted eyes were analyzed by normal phase HPLC, whereas Rho was measured spectrophotometrically. There were no differences in either 11-cis-retinal or Rho content found between PND40 and PND63 $Rho^{P23H/+}$ *or* $Rho^{+/+}$ mice. The mean amounts of 11-*cis*-retinal and Rho in PND40 and PND63 $Rho^{P23H/+}$ mouse eyes were about 25% of those in $Rho^{+/+}$ mice. Values are means ± SD. *n*, number of repeated analysis. *P*-values were determined by the student's *t*-test.

structure reveals a step in disc maturation, with small divided discs later fusing together to form mature discs. These divided discs are unlikely to result from a lower Rho concentration as the 2-fold reduction of Rho in $Rho^{+/-}$ mice results in short ROS, with both the diameter and the concentration of opsin per disc remaining unchanged (58).

Finally, we investigated whether the P23H opsin can be photoactivated and trigger phototransduction. Here, we found that the transretinal ERG responses from $Rho^{P23H/P23H}$ mice had the sensitivity and kinetics comparable with those of mouse cones (Fig. 11). Further analysis of P23H mutants in either rod- ($Gnat1^{-/-}$) or cone- ($Gnat2^{cpfl3/cpfl3}$) deficient mice allowed us to demonstrate that $Rho^{P23H/P23H}$ rods can produce light responses but with sensitivity that is ∼17 000-fold lower than that of $Rho^{+/+}$ rods. Thus, despite the grossly abnormal morphology of $Rho^{P23H/P23H}$ rods, the P23H opsin present in their outer segments can mediate phototransduction.

$Gnat2^{cpfl3/cpfl3}Rho^{P23H/P23H}$ retinas could contain a small residual cone component, ∼25% that of normal cones (60). Based on the maximal amplitudes of the responses from $Gnat1^{-/-}$ $Rho^{P23H/P23H}$ and $Gnat2^{cpfl3/cpfl3}Rho^{P23H/P23H}$ retinas, we estimate that the cone contribution to the overall response in the latter is not more than ∼30%, indicating that the responses are dominated by mutant rods. Thus, the response acceleration we observed in $Gnat2^{cpfl3/cpfl3}Rho^{P23H/P23H}$ retinas could not be explained by a cone contribution but instead, indicates a substantial acceleration of these responses from P23H rods.

Previously, it was suggested that phosphorylation and dephosphorylation of Rho in P23H transgenic rats are misregulated and that this represents a possible degenerative mechanism (61). Indeed, timely phosphorylation of photoactivated Rho is critical for the proper termination of the rod light response (62) and deficiencies in this reaction result in an abnormally slow response shutoff (63,64). Equally importantly, Rho phosphorylation deficiencies can result in photoreceptor degeneration (48,63,65,66).

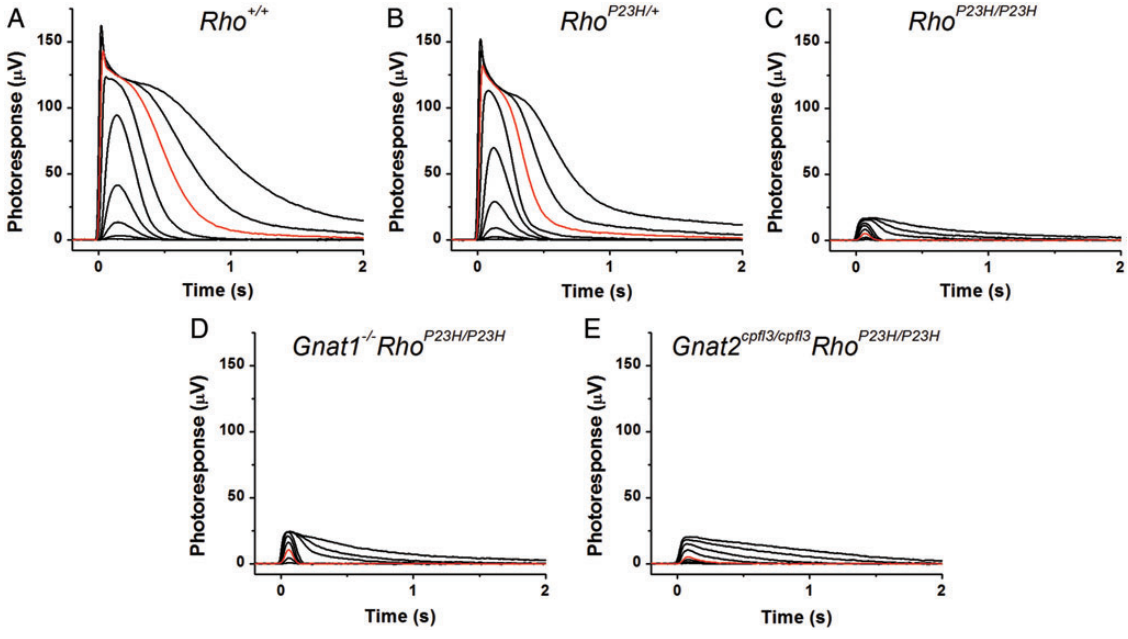

Figure 10. Transretinal ERG responses are shown from representative PND14-16 $Rho^{+/+}$ (**A**), $Rho^{P23H/+}$ (**B**), $Rho^{P23H/P23H}$ (**C**), $Gnat1^{-/-}Rho^{P23H/P23H}$ (**D**) and $Gnat2^{cpfl3/cpfl3}Rho^{P23H/P23H}$ (**E**) mouse retinas. Flash strengths of 505 nm light were increased stepwise from 0.5 to 3920 photons μm^{-2} ($Rho^{+/+}$ and $Rho^{P23H/+}$ mice), from 33.4 to 2.0×10^6 photons μm^{-2} ($Rho^{P23H/P23H}$ and $Gnat1^{-/-}Rho^{P23H/P23H}$ mice), and from 1190 to 5.7×10^6 photons μm^{-2} ($Gnat2^{cpfl3/cpfl3}Rho^{P23H/P23H}$ mice) by steps of 0.5 log units each. Red traces in (**A**)–(**D**) show responses to an identical light intensity of 392 photons μm^{-2} and the red trace in (**E**) corresponds to a light intensity of 5.7×10^5 photons μm^{-2} for comparison. In these five retinas, maximum responses were 124 μV (A), 117 μV (B), 17 μV (C), 23 μV (D), and 20 μV (E).

However, our recordings from $Rho^{P23H/P23H}$ rods in mice with a $Gnat2^{cpfl3/cpfl3}$ background demonstrated responses with accelerated shutoff kinetics compared with $Rho^{+/+}$ (Fig. 11), suggesting that Rho phosphorylation is not compromised by the P23H Rho. Thus, our data indicate that the lack of phosphorylation is not the cause for degeneration of $Rho^{P23H/P23H}$ mouse retinas.

In summary, P23H opsin knock-in mice that genetically and pathologically recapitulate common human adRP provided a wealth of new information about the etiology of this disease. Our detailed analyses highlight the possibility that a structural defect in ROS formation is a chief cause of retinal degeneration (summarized in Fig. 13). Because $Rho^{P23H/+}$ mice express both WT opsin and P23H opsin, sagittally oriented disc membranes are both enlarged (purple) and can retain this orientation as rods mature. These observations strongly indicate that P23H opsin interferes with the process of disc membrane reorientation. With this knowledge in hand, therapeutic approaches should be precisely geared toward alleviating this abnormal disc formation or stabilizing the abnormal ROS. These genetically altered mice highlight an intriguing new general step in normal disc formation by rod photoreceptor cells.

MATERIALS AND METHODS

Animals

Mice were raised in a 12 h light (127–255 lux)/12 h dark (<10 lux) cyclic environment at the Case Western Reserve University, School of Medicine animal facility where adult mice were maintained on a standard diet. C57BL/6 mice purchased from the Jackson Laboratory (Bar Harbor, ME, USA) were used as $Rho^{+/+}$ controls. Experimental $Rho^{P23H/P23H}$ and $Rho^{P23H/+}$ mice with C57BL/6J backgrounds (backcrossed with C57BL/6J mice for over six generations) were used both experimentally and for crossbreading with $Rho^{-/-}$ (4), $Gnat1^{-/-}$ (67) and $Gnat2^{cpfl3/cpfl3}$ (60) (B6.Cg-$Gnat2^{cpfl3}$/Boc, stock number: 6795, Jackson Laboratory) mice. None of these mice had either a Crb1 gene rd8 mutation (68) or a cGMP phosphodiesterase β-subunit gene rd1 mutation (69). All animal procedures and experiments were approved by the Case Western Reserve University Animal Care Committee or the Washington University Animal Studies Committee and conformed to the recommendations of both the American Veterinary Medical Association Panel on Euthanasia and the Association of Research for Vision and Ophthalmology.

Genotyping

Genotyping was performed by PCR with genomic DNA from mouse tails (20). Primer pairs for genotyping were as follows: rho^{P23H}, GenoRhoL 2163 and GenoRhoR 2561 (20); $mrho^{-}$ (Rho knock-out mutation), opsin exon 1_R, K183-F Opsin exon1_R and Opsin exon 1_F (20); $Gnat1^{-}$, K183, 5′-CTTGGCGAATATCATGGTGG-3′ and FH588, 5′-CACC AGCACCATGTCGTAAG-3′ (~600 bp); $Gnat1^{+}$, FH589, 5′-G TACACATGTAGATGCAGGAG-3′ and FH588 (~500 bp); $mCrb1^{rd8}$, mCrb1 mF2, mCrb1 mR and mCrb1 mF1 (68); $Pde6b^{rd1}$ (phosphodiesterase β-subunit gene rd1 mutation), W149 and W150 (69); and $Gnat2^{cpfl3}$, Gnat2-dF and Gnat 2-dR (60).

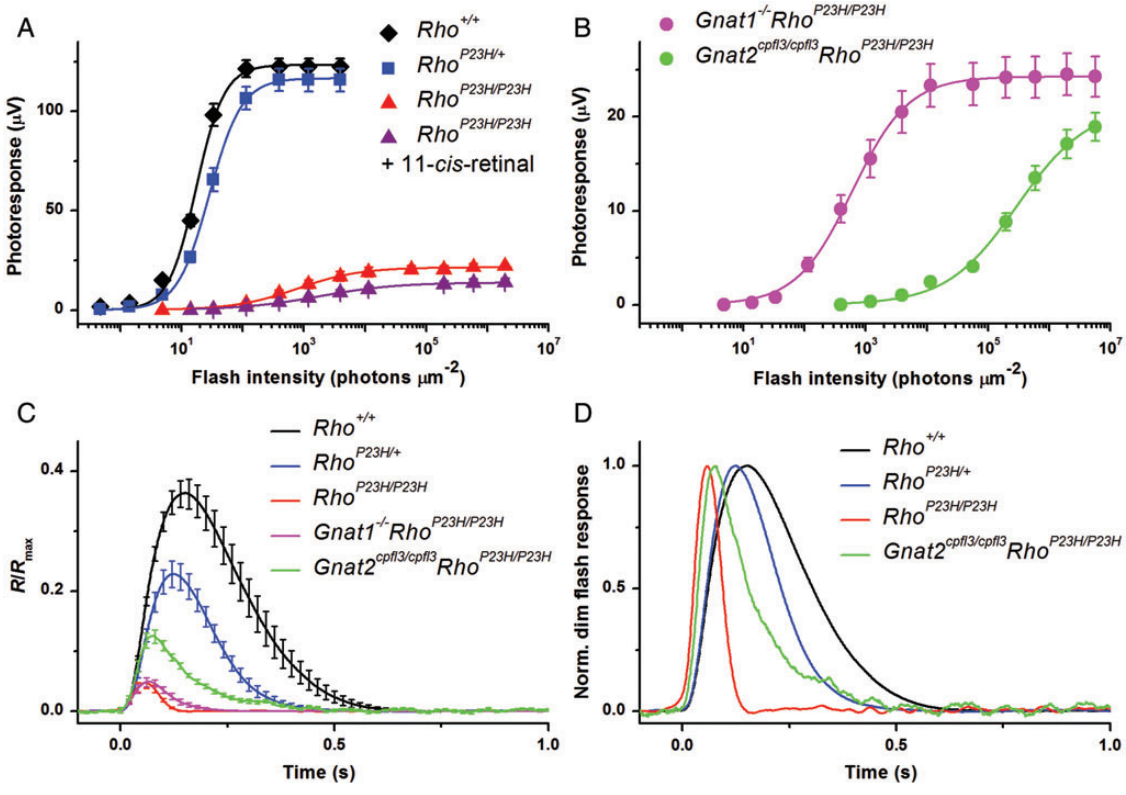

Figure 11. Characterization of transretinal ERG responses from five mouse lines. Absolute response amplitudes as a function of flash strength were obtained from PND14–16 $Rho^{+/+}$, $Rho^{P23H/+}$, $Rho^{P23H/P23H}$ (**A**), $Gnat1^{-/-}Rho^{P23H/P23H}$ and $Gnat2^{cpfl3/cpfl3}Rho^{P23H/P23H}$ (**B**) mouse retinas. Points were fitted with Naka-Rushton hyperbolic functions for $Rho^{+/+}$ ($n = 9$), $Rho^{P23H/+}$ ($n = 6$), $Rho^{P23H/P23H}$ ($n = 12$), $Gnat1^{-/-}Rho^{P23H/P23H}$ ($n = 11$) and $Gnat2^{cpfl3/cpfl3}Rho^{P23H/P23H}$ ($n = 11$) retinas. The intensity–response relationship also is shown as purple triangles in (A) for $Rho^{P23H/P23H}$ retinas treated with 130 μM 11-*cis*-retinal for 1 h at room temperature prior to recording ($n = 6$). (**C**) Amplification of the phototransduction cascade in mouse photoreceptors. Population-averaged dim flash responses to light intensities of 14 photons μm^{-2} (for $Rho^{+/+}$ and $Rho^{P23H/+}$ retinas), 392 photons μm^{-2} (for $Rho^{P23H/P23H}$ and $Gnat1^{-/-}Rho^{P23H/P23H}$ retinas) and 1.1×10^4 photons μm^{-2} (for $Gnat2^{cpfl3/cpfl3}Rho^{P23H/P23H}$ retinas) were normalized to their corresponding maximum dark voltages, R_{max}. Then, fractional responses were scaled down by factors of 1 ($Rho^{P23H/+}$ and $Gnat2^{cpfl3/cpfl3}Rho^{P23H/P23H}$) or 8 ($Rho^{P23H/P23H}$ and $Gnat1^{-/-}Rho^{P23H/P23H}$) to make all initial rising phases coincide with that of the $Rho^{+/+}$ response. Light intensities corresponding to these scaled responses were thus determined as $14/1 = 14$ photons μm^{-2} ($Rho^{P23H/+}$), $392/8 = 49$ photons μm^{-2} ($Rho^{P23H/P23H}$ and $Gnat1^{-/-}Rho^{P23H/P23H}$) and $1.1 \times 10^4/1 = 1.1 \times 10^4$ photons μm^{-2} ($Gnat2^{cpfl3/cpfl3}Rho^{P23H/P23H}$). (**D**) Kinetics of dim flash responses in mouse photoreceptors. Normalized population-averaged dim flash responses demonstrate the accelerated response inactivation in $Rho^{P23H/+}$, $Rho^{P23H/P23H}$ and $Gnat2^{cpfl3/cpfl3}Rho^{P23H/P23H}$ mouse retinas.

Transretinal ERG recordings

All mice in the five groups tested ($Rho^{+/+}$, $Rho^{P23H/+}$, $Rho^{P23H/P23H}$, $Gnat1^{-/-}Rho^{P23H/P23H}$ and $Gnat2^{cpfl3/cpfl3}$ $Rho^{P23H/P23H}$) were 14–16 days old. After dark-adaption overnight, animals were euthanized by CO_2 asphyxiation and their retinas were removed under infrared illumination. A whole single retina was mounted on filter paper with the photoreceptor side up and placed on the recording chamber with an electrode connected to its base. A second electrode was placed above the center of the retina and both electrodes were connected to a differential amplifier. The retina was perfused with Locke's solution (112.5 mM NaCl, 3.6 mM KCl, 2.4 mM $MgCl_2$, 1.2 mM $CaCl_2$, 10 mM 4-(2-hydroxyethyl)-1-piperazineethanesulfonic acid (HEPES), pH 7.4, 20 mM $NaHCO_3$, 3 mM Na succinate, 0.5 mM Na glutamate, 0.02 mM ethylenediaminetetraacetic acid (EDTA) and 10 mM glucose). The perfusion solution was supplemented with 2 mM L-glutamate and 10 μM DL-2-amino-4-phosphonobutyric acid (DL-AP4) to block synaptic components of the photo-response (70), 20 μM $BaCl_2$ to suppress the slow glial PIII component (71) and MEM vitamin and amino acid solutions (Sigma) to retain retinal viability. The solution was continuously bubbled with a 95% O_2/5% CO_2 mixture heated to 36–37°C. The lower electrode space solution (140 mM NaCl, 3.6 mM KCl, 2.4 mM $MgCl_2$, 1.2 mM $CaCl_2$, 3 mM HEPES, 10 mM glucose, pH 7.4) also contained 2 mM L-glutamate and 10 mM $BaCl_2$. A second retina was stored in oxygenated aqueous L15 (13.6 mg/ml, pH 7.4, Sigma) solution containing 0.1% bovine serum albumin at room temperature until used, typically within 15–20 min.

Light stimulation was applied as 20 ms test flashes of calibrated 505 nm LED light with its intensity controlled by neutral density filters and a computer in 0.5 log unit steps. Photoresponses were amplified by a differential amplifier (DP-311; Warner Instruments), low-pass filtered at 30 Hz (8-pole Bessel), digitized at 1 kHz and stored in a computer for further analysis. The intensity–response relationships were fitted with Naka–Rushton hyperbolic functions, as follows:

$$R = \frac{R_{max} \cdot I^n}{I^n + I_{1/2}^n}$$

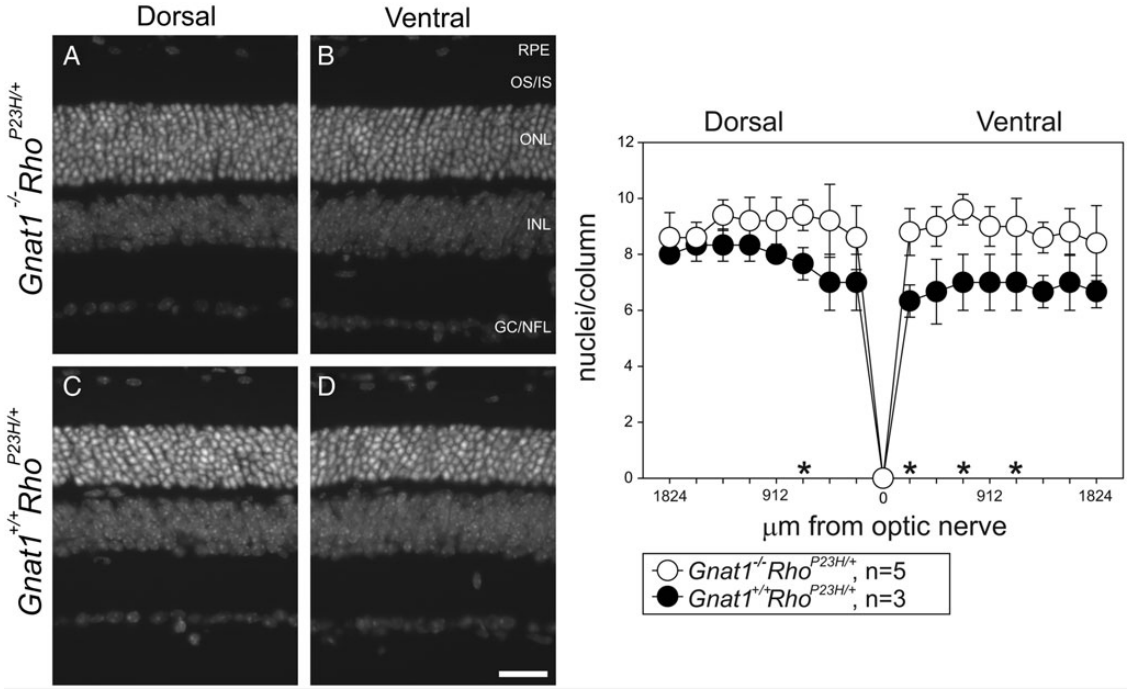

Figure 12. Numbers of photoreceptor nuclei in $Gnat1^{-/-}Rho^{P23H/+}$ and $Gnat1^{+/+}Rho^{P23H/+}$ mouse eyes indicate that retinal degeneration in $Rho^{P23H/+}$ mice is phototransduction independent. Because genetic deletion of *Gnat1* causes absence of rod phototransduction, numbers of photoreceptor nuclei per outer nuclear layer column were compared at PND35 in $Gnat1^{+/+}Rho^{P23H/+}$ and $Gnat1^{-/-}Rho^{P23H/+}$ mice (right). Nuclei in cryosections at 16 positions ranging from the optic nerve to the dorsal and ventral retina were counted (right). Four of the 16 positions indicated by * showed fewer nuclei in $Gnat1^{+/+}Rho^{P23H/+}$ mice than in $Gnat1^{-/-}Rho^{P23H/+}$ mice, $^*P < 0.01$, *t*-test. *P*-values for numbers at the four positions indicated by * were 0.008, 0.004, 0.008 and 0.008 from left (dorsal, 684 μm from the optic nerve) to right (ventral, 228, 684 and 1140 μm from the optic nerve). Numbers of nuclei measured at the remaining 12 positions were not statistically different. (**A**–**D**, left) Nuclear-stained cryosection images of the retina located 912 μm from the optic nerve (dorsal and ventral). $Gnat1^{-/-}Rho^{P23H/+}$ (A and B) and $Gnat1^{+/+}Rho^{P23H/+}$ (C and D). RPE, retinal pigmented epithelium; OS/IS, outer segment/inner segment; ONL, outer nuclear layer; INL, inner nuclear layer; and GC/NFL, ganglion cell/nerve fiber layer. Scale bar: 50 μm.

where R is the transient-peak amplitude of response, R_{max} is the maximal response amplitude, I is the flash intensity, n is the Hill coefficient (exponent) and $I_{1/2}$ is the half-saturating light intensity.

Application of exogenous 11-*cis*-retinal to $Rho^{P23H/P23H}$ retinas was performed as follows: 300 μg of dried retinoid was dissolved in 8 μl of ethanol and diluted to 8 ml with L15 solution containing 1% bovine serum albumin. The final 11-*cis*-retinal concentration was ∼130 μM, and that for ethanol was 0.1%. Retinas were incubated in this oxygenated solution for 1 h at room temperature before transfer to the perfusion chamber.

Retinoid analyses

Because the lengths of rod photoreceptor cell outer segments change when they are exposed to new illumination conditions (72), mice were kept under illumination conditions described above for 12–14 days prior to overnight dark adaptation (from 5–6 p.m. to 8 a.m.–2 p.m., 18–24 h). Retinoids were isolated from mouse eyes as previously described (46,73) with the following modifications. Mouse eyeballs were placed into cryo-storage tubes and immediately frozen in liquid nitrogen and kept at −80°C. Then after 1500 pmol of all-*trans*-retinyl acetate was added to each single eye retinal homogenate as an external standard, retinoids were extracted in hexane, dried in a vacuum concentrator (Savant SpeedVac, Thermo Fisher Scientific Inc., Waltham, MA, USA) and dissolved in 150–160 μl of hexane. Then 100 μl of this mixture was injected onto a high-pressure liquid chromatography (HPLC) column (5 μm silica, 4.6 × 250 mm, Beckman Coulter, Inc., Brea, CA, USA) connected to a normal phase HPLC (Agilent 1100 series, Agilent Technologies Inc.). After sample injection, the column was eluted with the following concentrations of ethyl acetate in hexane at a flow rate of 1.4 ml/min: 0.5% from 0 to 11 min; 1% from 11 to 18 min; and 6% from 18 to 60 min. Amounts of retinoids were determined from their peak absorption areas at 325 nm for all-*trans*-retinyl acetate (external standard) and at 360 nm for 11-*cis*-retinal oxime. Numbers of eyeballs per analysis were as follows: four or six eyes from PND14 $Rho^{+/-}$ and $Rho^{P23H/+}$ mice; two, four or six eyes from PND14 $Rho^{+/+}$ mice; four eyes from PND40 $Rho^{+/+}$ and $Rho^{P23H/+}$ mice; four eyes from PND63 $Rho^{P23H/+}$ mice; and two or four eyes from PND63 $Rho^{+/+}$ mice. Amounts of all-*trans*-retinal per eye in $Rho^{+/+}$ mice (mean ± SD) were 25.9 ± 4.1 pmol at PND40 and 29.0 ± 7.6 pmol at PND63. Mean amounts of all-*trans*-retinal in other mice of the same age and all PND14 mice were less than lower limit of detection (23 pmol/injection).

Calibration curves ($R^2 > 0.99$) for each retinoid were constructed as follows: 11-*cis*-retinal oxime, 19 standard points (100–10 000 pmol); all-*trans*-retinyl acetate, 16 standard points (1.1–17.7 nmol); and all-*trans*-retinal oxime, 19 standard points (12–3000 pmol). Each standard point was measured three to four times. To obtain more than 90% pure 11-*cis*-retinal oxime, 11-*cis*-retinal oxime was generated from fresh 11-*cis*-retinal (TRC, Toronto, Ontario, Canada) within 2 days of arrival.

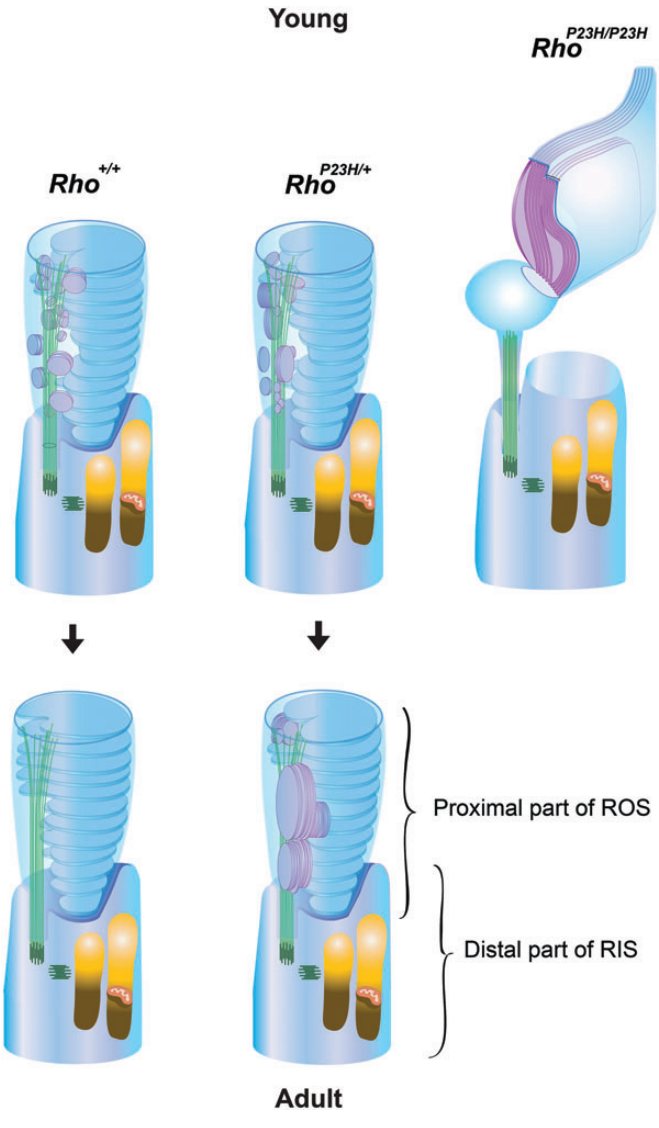

Figure 13. Diagram of primordial rod disc reorientation. In $Rho^{+/+}$ mice with normal copies of WT rhodopsin ($Rho^{+/+}$), sagittally oriented primordial discs (purple) were observed only in young rods. In adult rods, all disc membranes were oriented transversely (blue). These observations indicate that primordial discs shift from a sagittal to a transverse orientation. In $Rho^{P23H/+}$ mice that express both WT opsin and P23H opsin, sagittally oriented primordial disc membranes both enlarge (purple) and can retain their sagittal orientation as rods mature. These observations indicate that P23H opsin interferes with the process of disc membrane reorientation. That this is a dominant-negative effect is reinforced by the observation that primordial disc membranes containing only P23H opsin are incapable of orienting transversely ($Rho^{P23H/P23H}$, purple). Indeed, the combined evidence strongly indicates that primordial discs normally shift from a sagittal to transverse orientation in the rods of $Rho^{+/+}$ adult mice.

Rho determinations

After dark-adaptation overnight, mice were euthanized and their eyes were enucleated, the cornea and lens were removed and eyecups were frozen as described in the Retinoid Analyses section of Materials and Methods. Then one to eight frozen eye cups from $Rho^{+/+}$ mice or two to eight frozen eye cups from $Rho^{P23H/+}$ mice were transferred to 1.5 ml tubes and homogenized in 600 µl of 125 mM NaCl, 10 mM BisTris propane, pH 7.5, with a polytetrafluoroethylene (PTFE) pestle. After homogenization, 60 µl of 200 mM *n*-dodecyl-β-D-maltoside (DDM) was added and tubes in ice were shaken for 1 h on a shaking device (Nutator, Clay Adams Brand, Sparks, MD, USA). Supernatants obtained after a 98 384 g centrifugation for 30 min at 4°C were used for Rho absorbance measurements with a spectrophotometer (Cary 50, Agilent Technologies Inc., Santa Clara, CA, USA). Rho was bleached with 480–520 nm light for 6 min in the presence of 4.5 mM hydroxylamine, pH 7.0–7.5 (74). The concentration of Rho was determined from the absorption difference at 500 nm before and after bleaching and the Rho extinction coefficient $\in = 40\,600\ cm^{-2}$ per mole (74).

Photoreceptor nuclei counting

$Gnat1^{-/-}Rho^{P23H/+}$ and $Gnat1^{+/+}Rho^{P23H/+}$ mice were obtained from five internal breeding pairs of $Gnat1^{+/-}Rho^{P23H/+}$ mice. Because $Gnat1^{-/-}$ causes morphological retinal degeneration by 13 weeks but not at 4 weeks of age (67), numbers of photoreceptor nuclei were analyzed at PND35. Eyecups were fixed with 4% paraformaldehyde in 5% sucrose containing phosphate-buffered saline (PBS: 136 mM NaCl, 2 mM KCl, 8 mM, Na_2HPO_4, 1 mM KH_2PO_4, pH 7.4) for 5 h at 4°C. After fixation, eye cups were washed in 5% sucrose containing PBS and then were dehydrated with increasing concentrations of sucrose in PBS at 4°C (75). After dehydration in 20% sucrose containing PBS, eye cups were infiltrated with mixture of O.C.T. compound (Sakura Finetek, Tokyo, Japan) and 20% sucrose containing PBS (75) and then frozen. Cryo-sections (5–7 µm) across the dorsal-ventral axis were made with a cryostat-microtome (CM1850, Leica, Bannockburn, IL, USA) and nuclei were labeled with 12.3 µg/ml of Hoechst 33 342 (Invitrogen). Images of Hoechst 33342-labeled nuclei were acquired with a fluorescence microscope (CTR 6000, Leica) connected to a CCD camera (QImaging Retiga Exi Fast 1394, QImaging, Surrey, British Columbia, Canada). To count nuclei, the ONL of an entire retina in the ×5 objective lens image was initially marked at 228 µm intervals with a dashed line using the 'dotted line' plug-in of ImageJ software (National Institutes of Health). Then, the number of nuclei at the corresponding positions in the ×20 objective lens image were manually counted with the 'cell counter' plug-in of ImageJ software.

Immunohistochemistry

Cryo-sections (7–8 µm) of eye cups were prepared as described above and processed as described previously (20). Final concentrations of antibodies were as follows: mouse 1D4 (5 µg/ml); rat 13A4 anti-prominin 1 (0.94 µg/ml, from Dr Corbeil) (76); rabbit anti-calreticulin (1:250, Sigma); rabbit anti-GORASP2 (1:10, Proteintech); Alexa 488 goat anti-mouse IgG (3 µg/ml, Molecular Probes); Cy3-conjugated goat anti-rat IgG (3 µg/ml, Jackson ImmunoResearch, West Grove, PA, USA); Cy3-conjugated goat anti-rabbit IgG (3 µg/ml, Jackson ImmunoResearch, West Grove, PA, USA). Samples were prepared from three mice for each genotype. Immunofluorescent labeled sections were analyzed with either a fluorescence microscope (CTR 6000, Leica) or confocal microscopes (TCS SP2 and SP5, Leica). For each experiment, no cross-talk was analyzed by single immuno-labeling and non-specific reactions were analyzed

by a negative control without primary antibody. The confocal microscopy images (Fig. 1A and B) were maximum projection images of 14 stacks of images corrected from 3.21 μm thick optical sections. The confocal microscopy images (Fig. 1C–H) were maximum projection images of 14 stacks of images corrected from 4.5 μm thick optical sections.

Transmission EM

Mouse eyecups were first fixed with half-strength Karnovsky's fixative (77) in 2.5% DMSO (78) containing 0.037 M Millonig's buffer (79) for 20 min to 3 h at room temperature, cut in half on either their dorsal-ventral axis (left eye) or nasal-temporal axis (right eye), and then fixed again for 2 h at 37°C. After a 0.1 M monobasic-dibasic sodium phosphate buffer, pH 7.4, rinse, half-eyecups were post-fixed with ferrocyanide-reduced osmium tetroxide for 2 h at room temperature with one osmium solution change. Following a distilled water rinse, half-eyecups were stained overnight with 0.25% uranyl acetate at 4°C. Stained half-eyecups were rinsed with distilled water and then dehydrated with a series of increasing ethanol concentrations in distilled water followed by increasing propylene oxide concentrations in ethanol. After dehydration with 100% propylene oxide, half eyecups were infused with a series of increasing epoxy (Poly/Bed® 812 Embedding Media, Polysciences, Inc., Warrington, PA, USA) concentrations in propylene oxide. Following infiltration with 100% epoxy, half-eyecups were polymerized at 70°C for 4 days and the resulting blocks were sectioned with an ultramicrotome (MT6000-XL, RMC, Inc., Tucson, AZ, USA). Thick sections (~500 nm) were stained with 0.5% toluidine blue O (Sigma) to observe morphology at a light microscopy level (Fig. 1I and J). Thin sections (~80 nm) were stained with 2% uranyl acetate in 50% methanol (80) followed by staining with modified Sato's lead-staining solution (81) with the following modification: lead citrate was employed instead of calcinized lead citrate. After staining, thin sections were coated with carbon (DV-401, Denton Vacuum, LLC, Moorestown, NJ, USA). Samples were observed with either a JEOL 1200 EX EM at 80 kV (JEOL, Musashino, Tokyo, Japan) or a Tecnai G2 Spirit BioTwin EM at 100 kV (FEI, Hillsboro, Oregon).

Immuno-EM

Mouse eyecups were fixed with 4% paraformaldehyde, 0.05% glutaraldehyde, 0.001% DMSO, 0.00025% $CaCl_2$ and 0.00025% $MgCl_2$ in 0.185 M Millonig's buffer (79) for 0.5–4 h at room temperature, cut in quarters with a blade and then fixed again for 0.5 h at 37°C. After fixation, eyecup quarters were rinsed with an increasing series of Millong's buffer (0.22 M Millonig's buffer containing 50 mM glycine for 5 min, 0.23 M Millonig's buffer three times for 5 min each and 0.24 M Millonig's buffer for 5 min). Samples were then dehydrated with a series of increasing ethanol concentrations (30, 50 and 70%). After dehydration with 70% ethanol, resulting samples were infiltrated with LR White Resin, Medium Grade (London Resin Co Ltd, Berkshire, UK) in 95% ethanol at ratios of 1:1 and 2:1 at −20°C. After eyecup quarters were infiltrated with 100% LR White Resin, further infiltration was accomplished overnight at 4°C, 1.5 h at room temperature and 2 h in vacuum desiccators with a double change of resin. Eyecup quarters then were polymerized at 40°C for 5 days. Thin sections (~80 nm) collected on nickel grids were processed as described in ref. (82) with the following modifications: sections were blocked with 5% dry milk (CARNATION® Milk, Nestlé, Vevey, Switzerland) in PBST (1% bovine serum albumin, 0.01% Tween 20 in PBS, pH 7.4), for 20 min at room temperature and then incubated with primary antibodies for 1 h at 37°C or overnight at 4°C at the following dilutions: 1D4 (5 mg/ml) (83), 1:50 and 4D2 [Hybridoma Supernatant, kindly provided by Dr Molday (84)], 1:10. Then after a rinse in PBST, samples were incubated with 5 nm gold particle-conjugated anti-mouse IgG (BBI, Cardiff, UK) secondary antibody at a 1:30 dilution for 1.5 h at room temperature. For negative controls, sections were incubated with secondary antibody only. Such negative controls were always processed together with experimental samples and the former were checked for possible signals. But this procedure did not preserve membrane structures well, primarily because osmium post-fixation was lacking. Thus, we imaged immuno-EM samples with STEM instead of TEM. Because capturing 5 nm particle signals on the retina is difficult with either STEM or TEM at 200 kV, we first analyzed immuno-EM samples with TEM at 80 kV (JEOL 1200Ex) to map signal regions on the retina, and then imaged the corresponding regions with STEM at 200 kV (Libra 200FE, Carl Zeiss, Oberkochen, Germany).

Statistical analyses

Data for all experiments are expressed as means ± standard deviations of the mean (SDM). The independent two-tailed Student's *t*-test was used to analyze the data, with accepted significance set at $P < 0.05$ (electrophysiology) and $P < 0.01$ for other analyses.

ACKNOWLEDGMENTS

We thank Dr Leslie T. Webster Jr (Case Western Reserve University, CWRU), Dr. Thomas Sundermeier and other members of Palczewski's laboratory for helpful comments on this manuscript; Dr Zhiqian Dong (Polgenix Inc., Cleveland) and David Peck (CWRU) for technical help. We also thank Dr Beata Jastrzebska (CWRU) for helpful instruction about the Rho measurements; Dr Marcin Golczak and Dr Hideo Kohno (CWRU) for their helpful instruction for retinoid analysis; Dr Akiko Maeda and Dr Tadao Maeda (CWRU) for their assistance with HPLC analyses; Dr Hisashi Fujioka (CWRU) for helpful instruction and suggestions for EM sample preparations and TEM imaging; Kiet Luc and Dr Hitomi Midori (CWRU) for their technical assistance on printing and developing of negatives; Heather Holdaway (Cleveland Center for Membrane and Structural Biology, CWRU) for instructions in TEM imagining and Dr Denis Corbeil (Max-Planck-Institute, Dresden, Germany) for anti-prominin 1 antibodies; Philip Ropelewski and Richard Lee for helpful instruction and assistance for SP2 confocal microscope imaging; Reza Shaghi-Moshtaghin (Swagelok Center for Surface Analysis of Materials, CWRU) for helpful instruction for STEM imaging. We also thank Dr Janis Lem (Tufts University) for $Rho^{-/-}$ and $Gnat1^{-/-}$ mice; Dr Robert S. Molday (University of British Columbia, Vancouver, Canada) for 4D2 antibodies; and Dr David Salom (Polgenix Inc.) for 1D4 antibodies.

Conflict of Interest statement. None declared.

FUNDING

This work was supported by funding by the grants R01EY009339 (K.P.), R24EY021126 (K.P., V.K.), R01EY019312 (V.K.), EY002687 to the Department of Ophthalmology and Visual Sciences at Washington University, and P30EY11373 from the National Eye Institute of the National Institutes of Health (NIH), and Research to Prevent Blindness and Foundation Fighting Blindness. The Jackson laboratory (Bar Harbor, ME) was supported from the Mouse Mutant Resource and NIH project numbers OD010972-35, OD011163-02, RR001183 and RR032339. K.P. is John H. Hord Professor of Pharmacology.

REFERENCES

1. Young, R.W. (1983) The ninth Frederick H. Verhoeff lecture. The life history of retinal cells. *Trans. Am. Ophthalmol. Soc.*, **81**, 193–228.
2. Palczewski, K. (2012) Chemistry and biology of vision. *J. Biol. Chem.*, **287**, 1612–1619.
3. Palczewski, K. (2006) G protein-coupled receptor rhodopsin. *Annu. Rev. Biochem.*, **75**, 743–767.
4. Lem, J., Krasnoperova, N.V., Calvert, P.D., Kosaras, B., Cameron, D.A., Nicolo, M., Makino, C.L. and Sidman, R.L. (1999) Morphological, physiological, and biochemical changes in rhodopsin knockout mice. *Proc. Natl Acad. Sci. USA*, **96**, 736–741.
5. Humphries, M.M., Rancourt, D., Farrar, G.J., Kenna, P., Hazel, M., Bush, R.A., Sieving, P.A., Sheils, D.M., McNally, N., Creighton, P. *et al.* (1997) Retinopathy induced in mice by targeted disruption of the rhodopsin gene. *Nat. Genet.*, **15**, 216–219.
6. Wen, X.H., Shen, L., Brush, R.S., Michaud, N., Al-Ubaidi, M.R., Gurevich, V.V., Hamm, H.E., Lem, J., Dibenedetto, E., Anderson, R.E. *et al.* (2009) Overexpression of rhodopsin alters the structure and photoresponse of rod photoreceptors. *Biophys. J.*, **96**, 939–950.
7. Arshavsky, V.Y., Lamb, T.D. and Pugh, E.N. Jr. (2002) G proteins and phototransduction. *Annu. Rev. Physiol.*, **64**, 153–187.
8. Yau, K.W. and Hardie, R.C. (2009) Phototransduction motifs and variations. *Cell*, **139**, 246–264.
9. Sung, C.H., Davenport, C.M., Hennessey, J.C., Maumenee, I.H., Jacobson, S.G., Heckenlively, J.R., Nowakowski, R., Fishman, G., Gouras, P. and Nathans, J. (1991) Rhodopsin mutations in autosomal dominant retinitis pigmentosa. *Proc. Natl Acad. Sci. USA*, **88**, 6481–6485.
10. Dryja, T.P., McGee, T.L., Hahn, L.B., Cowley, G.S., Olsson, J.E., Reichel, E., Sandberg, M.A. and Berson, E.L. (1990) Mutations within the rhodopsin gene in patients with autosomal dominant retinitis pigmentosa. *N. Engl. J. Med.*, **323**, 1302–1307.
11. Noorwez, S.M., Kuksa, V., Imanishi, Y., Zhu, L., Filipek, S., Palczewski, K. and Kaushal, S. (2003) Pharmacological chaperone-mediated in vivo folding and stabilization of the P23H-opsin mutant associated with autosomal dominant retinitis pigmentosa. *J. Biol. Chem.*, **278**, 14442–14450.
12. Sung, C.H., Schneider, B.G., Agarwal, N., Papermaster, D.S. and Nathans, J. (1991) Functional heterogeneity of mutant rhodopsins responsible for autosomal dominant retinitis pigmentosa. *Proc. Natl Acad. Sci. USA*, **88**, 8840–8844.
13. Lin, J.H., Li, H., Yasumura, D., Cohen, H.R., Zhang, C., Panning, B., Shokat, K.M., Lavail, M.M. and Walter, P. (2007) IRE1 signaling affects cell fate during the unfolded protein response. *Science*, **318**, 944–949.
14. Tam, B.M. and Moritz, O.L. (2006) Characterization of rhodopsin P23H-induced retinal degeneration in a Xenopus laevis model of retinitis pigmentosa. *Invest. Ophthalmol. Vis. Sci.*, **47**, 3234–3241.
15. Gorbatyuk, M.S., Knox, T., LaVail, M.M., Gorbatyuk, O.S., Noorwez, S.M., Hauswirth, W.W., Lin, J.H., Muzyczka, N. and Lewin, A.S. (2010) Restoration of visual function in P23H rhodopsin transgenic rats by gene delivery of BiP/Grp78. *Proc. Natl Acad. Sci. USA*, **107**, 5961–5966.
16. Lin, J.H. and Lavail, M.M. (2010) Misfolded proteins and retinal dystrophies. *Adv. Exp. Med. Biol.*, **664**, 115–121.
17. Lobanova, E.S., Finkelstein, S., Skiba, N.P. and Arshavsky, V.Y. (2013) Proteasome overload is a common stress factor in multiple forms of inherited retinal degeneration. *Proc. Natl Acad. Sci. USA*, **110**, 9986–9991.
18. Wu, T.H., Ting, T.D., Okajima, T.I., Pepperberg, D.R., Ho, Y.K., Ripps, H. and Naash, M.I. (1998) Opsin localization and rhodopsin photochemistry in a transgenic mouse model of retinitis pigmentosa. *Neuroscience*, **87**, 709–717.
19. Green, E.S., Menz, M.D., LaVail, M.M. and Flannery, J.G. (2000) Characterization of rhodopsin mis-sorting and constitutive activation in a transgenic rat model of retinitis pigmentosa. *Invest. Ophthalmol. Vis. Sci.*, **41**, 1546–1553.
20. Sakami, S., Maeda, T., Bereta, G., Okano, K., Golczak, M., Sumaroka, A., Roman, A.J., Cideciyan, A.V., Jacobson, S.G. and Palczewski, K. (2011) Probing mechanisms of photoreceptor degeneration in a new mouse model of the common form of autosomal dominant retinitis pigmentosa due to P23H opsin mutations. *J. Biol. Chem.*, **286**, 10551–10567.
21. Tam, B.M., Qazalbash, A., Lee, H.C. and Moritz, O.L. (2010) The dependence of retinal degeneration caused by the rhodopsin P23H mutation on light exposure and vitamin a deprivation. *Invest. Ophthalmol. Vis. Sci.*, **51**, 1327–1334.
22. Tam, B.M. and Moritz, O.L. (2007) Dark rearing rescues P23H rhodopsin-induced retinal degeneration in a transgenic Xenopus laevis model of retinitis pigmentosa: a chromophore-dependent mechanism characterized by production of N-terminally truncated mutant rhodopsin. *J. Neurosci.*, **27**, 9043–9053.
23. Lee, D.C., Vazquez-Chona, F.R., Ferrell, W.D., Tam, B.M., Jones, B.W., Marc, R.E. and Moritz, O.L. (2012) Dysmorphic photoreceptors in a P23H mutant rhodopsin model of retinitis pigmentosa are metabolically active and capable of regenerating to reverse retinal degeneration. *J. Neurosci.*, **32**, 2121–2128.
24. Haeri, M. and Knox, B.E. (2012) Rhodopsin mutant P23H destabilizes rod photoreceptor disk membranes. *PLoS ONE*, **7**, e30101.
25. LaVail, M.M., Yasumura, D., Matthes, M.T., Drenser, K.A., Flannery, J.G., Lewin, A.S. and Hauswirth, W.W. (2000) Ribozyme rescue of photoreceptor cells in P23H transgenic rats: long-term survival and late-stage therapy. *Proc. Natl Acad. Sci. USA*, **97**, 11488–11493.
26. Olsson, J.E., Gordon, J.W., Pawlyk, B.S., Roof, D., Hayes, A., Molday, R.S., Mukai, S., Cowley, G.S., Berson, E.L. and Dryja, T.P. (1992) Transgenic mice with a rhodopsin mutation (Pro23His): a mouse model of autosomal dominant retinitis pigmentosa. *Neuron*, **9**, 815–830.
27. Price, B.A., Sandoval, I.M., Chan, F., Simons, D.L., Wu, S.M., Wensel, T.G. and Wilson, J.H. (2011) Mislocalization and degradation of human P23H-rhodopsin-GFP in a knockin mouse model of retinitis pigmentosa. *Invest. Ophthalmol. Vis. Sci.*, **52**, 9728–9736.
28. Naash, M.I., Hollyfield, J.G., al-Ubaidi, M.R. and Baehr, W. (1993) Simulation of human autosomal dominant retinitis pigmentosa in transgenic mice expressing a mutated murine opsin gene. *Proc. Natl Acad. Sci. USA*, **90**, 5499–5503.
29. Oprian, D.D. (1992) Molecular determinants of spectral properties and signal transduction in the visual pigments. *Curr. Opin. Neurobiol.*, **2**, 428–432.
30. Kaushal, S. and Khorana, H.G. (1994) Structure and function in rhodopsin. 7. Point mutations associated with autosomal dominant retinitis pigmentosa. *Biochemistry*, **33**, 6121–6128.
31. Roof, D.J., Adamian, M. and Hayes, A. (1994) Rhodopsin accumulation at abnormal sites in retinas of mice with a human P23H rhodopsin transgene. *Invest. Ophthalmol. Vis. Sci.*, **35**, 4049–4062.
32. Lewin, A.S., Drenser, K.A., Hauswirth, W.W., Nishikawa, S., Yasumura, D., Flannery, J.G. and LaVail, M.M. (1998) Ribozyme rescue of photoreceptor cells in a transgenic rat model of autosomal dominant retinitis pigmentosa. *Nat. Med.*, **4**, 967–971.
33. Petters, R.M., Alexander, C.A., Wells, K.D., Collins, E.B., Sommer, J.R., Blanton, M.R., Rojas, G., Hao, Y., Flowers, W.L., Banin, E. *et al.* (1997) Genetically engineered large animal model for studying cone photoreceptor survival and degeneration in retinitis pigmentosa. *Nat. Biotechnol.*, **15**, 965–970.
34. Griciuc, A., Aron, L., Roux, M.J., Klein, R., Giangrande, A. and Ueffing, M. (2010) Inactivation of VCP/ter94 suppresses retinal pathology caused by misfolded rhodopsin in Drosophila. *PLoS Genet.*, **6**, e1001075.
35. Kosmaoglou, M., Schwarz, N., Bett, J.S. and Cheetham, M.E. (2008) Molecular chaperones and photoreceptor function. *Prog. Retin. Eye Res.*, **27**, 434–449.

36. Zhang, R., Oglesby, E. and Marsh-Armstrong, N. (2008) Xenopus laevis P23H rhodopsin transgene causes rod photoreceptor degeneration that is more severe in the ventral retina and is modulated by light. *Exp. Eye Res.*, **86**, 612–621.
37. Ross, J.W., Fernandez de Castro, J.P., Zhao, J., Samuel, M., Walters, E., Rios, C., Bray-Ward, P., Jones, B.W., Marc, R.E., Wang, W. *et al.* (2012) Generation of an inbred miniature pig model of retinitis pigmentosa. *Invest. Ophthalmol. Vis. Sci.*, **53**, 501–507.
38. Cuenca, N., Pinilla, I., Sauve, Y., Lu, B., Wang, S. and Lund, R.D. (2004) Regressive and reactive changes in the connectivity patterns of rod and cone pathways of P23H transgenic rat retina. *Neuroscience*, **127**, 301–317.
39. Steinberg, R.H., Fisher, S.K. and Anderson, D.H. (1980) Disc morphogenesis in vertebrate photoreceptors. *J. Comp. Neurol.*, **190**, 501–508.
40. Obata, S. and Usukura, J. (1992) Morphogenesis of the photoreceptor outer segment during postnatal development in the mouse (BALB/c) retina. *Cell Tissue Res.*, **269**, 39–48.
41. Chuang, J.Z., Zhao, Y. and Sung, C.H. (2007) SARA-regulated vesicular targeting underlies formation of the light-sensing organelle in mammalian rods. *Cell*, **130**, 535–547.
42. Zhang, Y., Molday, L.L., Molday, R.S., Sarfare, S.S., Woodruff, M.L., Fain, G.L., Kraft, T.W. and Pittler, S.J. (2009) Knockout of GARPs and the beta-subunit of the rod cGMP-gated channel disrupts disk morphogenesis and rod outer segment structural integrity. *J. Cell Sci.*, **122**, 1192–1200.
43. Yang, Z., Chen, Y., Lillo, C., Chien, J., Yu, Z., Michaelides, M., Klein, M., Howes, K.A., Li, Y., Kaminoh, Y. *et al.* (2008) Mutant prominin 1 found in patients with macular degeneration disrupts photoreceptor disk morphogenesis in mice. *J. Clin. Invest.*, **118**, 2908–2916.
44. Liu, Q., Lyubarsky, A., Skalet, J.H., Pugh, E.N. Jr. and Pierce, E.A. (2003) RP1 is required for the correct stacking of outer segment discs. *Invest. Ophthalmol. Vis. Sci.*, **44**, 4171–4183.
45. Jansen, H.G. and Sanyal, S. (1984) Development and degeneration of retina in rds mutant mice: electron microscopy. *J. Comp. Neurol.*, **224**, 71–84.
46. Palczewski, K., Van Hooser, J.P., Garwin, G.G., Chen, J., Liou, G.I. and Saari, J.C. (1999) Kinetics of visual pigment regeneration in excised mouse eyes and in mice with a targeted disruption of the gene encoding interphotoreceptor retinoid-binding protein or arrestin. *Biochemistry*, **38**, 12012–12019.
47. Zocher, M., Fung, J.J., Kobilka, B.K. and Muller, D.J. (2012) Ligand-specific interactions modulate kinetic, energetic, and mechanical properties of the human beta(2) adrenergic receptor. *Structure*, **20**, 1391–1402.
48. Fan, J., Sakurai, K., Chen, C.K., Rohrer, B., Wu, B.X., Yau, K.W., Kefalov, V. and Crouch, R.K. (2010) Deletion of GRK1 causes retina degeneration through a transducin-independent mechanism. *J. Neurosci.*, **30**, 2496–2503.
49. Sakurai, K., Chen, J. and Kefalov, V.J. (2011) Role of guanylyl cyclase modulation in mouse cone phototransduction. *J. Neurosci.*, **31**, 7991–8000.
50. Hoffmeister, H., Babinger, K., Gurster, S., Cedzich, A., Meese, C., Schadendorf, K., Osten, L., de Vries, U., Rascle, A. and Witzgall, R. (2011) Polycystin-2 takes different routes to the somatic and ciliary plasma membrane. *J. Cell Biol.*, **192**, 631–645.
51. Gilliam, J.C. and Wensel, T.G. (2011) TRP channel gene expression in the mouse retina. *Vision Res.*, **51**, 2440–2452.
52. Jansen, H.G., Sanyal, S., De Grip, W.J. and Schalken, J.J. (1987) Development and degeneration of retina in rds mutant mice: ultraimmunohistochemical localization of opsin. *Exp. Eye Res.*, **44**, 347–361.
53. De Robertis, E. (1956) Morphogenesis of the retinal rods; an electron microscope study. *J. Biophys. Biochem. Cytol.*, **2**, 209–218.
54. De Robertis, E. (1960) Some observations on the ultrastructure and morphogenesis of photoreceptors. *J. Gen. Physiol.*, **43**(6 suppl.), 1–13.
55. Weidman, T.A. and Kuwabara, T. (1968) Postnatal development of the rat retina. An electron microscopic study. *Arch. Ophthalmol.*, **79**, 470–484.
56. Zhao, Y., Hong, D.H., Pawlyk, B., Yue, G., Adamian, M., Grynberg, M., Godzik, A. and Li, T. (2003) The retinitis pigmentosa GTPase regulator (RPGR)-interacting protein: subserving RPGR function and participating in disk morphogenesis. *Proc. Natl Acad. Sci. USA*, **100**, 3965–3970.
57. Carter-Dawson, L.D. and LaVail, M.M. (1979) Rods and cones in the mouse retina. I. Structural analysis using light and electron microscopy. *J. Comp. Neurol.*, **188**, 245–262.
58. Liang, Y., Fotiadis, D., Maeda, T., Maeda, A., Modzelewska, A., Filipek, S., Saperstein, D.A., Engel, A. and Palczewski, K. (2004) Rhodopsin signaling and organization in heterozygote rhodopsin knockout mice. *J. Biol. Chem.*, **279**, 48189–48196.
59. Nickell, S., Park, P.S., Baumeister, W. and Palczewski, K. (2007) Three-dimensional architecture of murine rod outer segments determined by cryoelectron tomography. *J. Cell Biol.*, **177**, 917–925.
60. Chang, B., Dacey, M.S., Hawes, N.L., Hitchcock, P.F., Milam, A.H., Atmaca-Sonmez, P., Nusinowitz, S. and Heckenlively, J.R. (2006) Cone photoreceptor function loss-3, a novel mouse model of achromatopsia due to a mutation in Gnat2. *Invest. Ophthalmol. Vis. Sci.*, **47**, 5017–5021.
61. Saito, Y., Ohguro, H., Ohguro, I., Sato, N., Ishikawa, F., Yamazaki, H., Metoki, T., Ito, T. and Nakazawa, M. (2008) Misregulation of rhodopsin phosphorylation and dephosphorylation found in P23H rat retinal degeneration. *Clin. Ophthalmol.*, **2**, 821–828.
62. Palczewski, K., Rispoli, G. and Detwiler, P.B. (1992) The influence of arrestin (48 K protein) and rhodopsin kinase on visual transduction. *Neuron*, **8**, 117–126.
63. Chen, C.K., Burns, M.E., Spencer, M., Niemi, G.A., Chen, J., Hurley, J.B., Baylor, D.A. and Simon, M.I. (1999) Abnormal photoresponses and light-induced apoptosis in rods lacking rhodopsin kinase. *Proc. Natl Acad. Sci. USA*, **96**, 3718–3722.
64. Cideciyan, A.V., Zhao, X., Nielsen, L., Khani, S.C., Jacobson, S.G. and Palczewski, K. (1998) Null mutation in the rhodopsin kinase gene slows recovery kinetics of rod and cone phototransduction in man. *Proc. Natl Acad. Sci. USA*, **95**, 328–333.
65. Kristaponyte, I., Hong, Y., Lu, H. and Shieh, B.H. (2012) Role of rhodopsin and arrestin phosphorylation in retinal degeneration of Drosophila. *J. Neurosci.*, **32**, 10758–10766.
66. Maeda, T., Imanishi, Y. and Palczewski, K. (2003) Rhodopsin phosphorylation: 30 years later. *Prog. Retin. Eye Res.*, **22**, 417–434.
67. Calvert, P.D., Krasnoperova, N.V., Lyubarsky, A.L., Isayama, T., Nicolo, M., Kosaras, B., Wong, G., Gannon, K.S., Margolskee, R.F., Sidman, R.L. *et al.* (2000) Phototransduction in transgenic mice after targeted deletion of the rod transducin alpha -subunit. *Proc. Natl Acad. Sci. USA*, **97**, 13913–13918.
68. Mattapallil, M.J., Wawrousek, E.F., Chan, C.C., Zhao, H., Roychoudhury, J., Ferguson, T.A. and Caspi, R.R. (2012) The Rd8 mutation of the Crb1 gene is present in vendor lines of C57BL/6N mice and embryonic stem cells, and confounds ocular induced mutant phenotypes. *Invest. Ophthalmol. Vis. Sci.*, **53**, 2921–2927.
69. Pittler, S.J. and Baehr, W. (1991) Identification of a nonsense mutation in the rod photoreceptor cGMP phosphodiesterase beta-subunit gene of the rd mouse. *Proc. Natl Acad. Sci. USA*, **88**, 8322–8326.
70. Sillman, A.J., Ito, H. and Tomita, T. (1969) Studies on the mass receptor potential of the isolated frog retina. I. General properties of the response. *Vision Res.*, **9**, 1435–1442.
71. Nymark, S., Heikkinen, H., Haldin, C., Donner, K. and Koskelainen, A. (2005) Light responses and light adaptation in rat retinal rods at different temperatures. *J. Physiol.*, **567**, 923–938.
72. Schremser, J.L. and Williams, T.P. (1995) Rod outer segment (ROS) renewal as a mechanism for adaptation to a new intensity environment. I. Rhodopsin levels and ROS length. *Exp. Eye Res.*, **61**, 17–23.
73. Garwin, G.G. and Saari, J.C. (2000) High-performance liquid chromatography analysis of visual cycle retinoids. *Methods Enzymol.*, **316**, 313–324.
74. Wald, G. and Brown, P.K. (1953) The molar extinction of rhodopsin. *J. Gen. Physiol.*, **37**, 189–200.
75. Barthel, L.K. and Raymond, P.A. (1990) Improved method for obtaining 3-microns cryosections for immunocytochemistry. *J. Histochem. Cytochem.*, **38**, 1383–1388.
76. Weigmann, A., Corbeil, D., Hellwig, A. and Huttner, W.B. (1997) Prominin, a novel microvilli-specific polytopic membrane protein of the apical surface of epithelial cells, is targeted to plasmalemmal protrusions of non-epithelial cells. *Proc. Natl Acad. Sci. USA*, **94**, 12425–12430.
77. Karnovsky, M.J. (1965) A formaldehyde-glutaraldehyde fixative of high osmolality for use in electron microscopy. *J. Cell Biol.*, **27**, 137A.
78. Kalt, M.R. and Tandler, B. (1971) A study of fixation of early amphibian embryos for electron microscopy. *J. Ultrastruct. Res.*, **36**, 633–645.
79. Millonig, G. (1961) Advantages of a phosphate buffer for OsO_4 solutions in fixation. *J. Appl. Phys.*, **32**, 1637.
80. Tandler, B. (1990) Improved uranyl acetate staining for electron microscopy. *J. Electron Microsc. Tech.*, **16**, 81–82.

81. Hanaichi, T., Sato, T., Iwamoto, T., Malavasi-Yamashiro, J., Hoshino, M. and Mizuno, N. (1986) A stable lead by modification of Sato's method. *J. Electron Microsc. (Tokyo)*, **35**, 304–306.
82. Fujioka, H., Moghaddas, S., Murdock, D.G., Lesnefsky, E.J., Tandler, B. and Hoppel, C.L. (2011) Decreased cytochrome c oxidase subunit VIIa in aged rat heart mitochondria: immunocytochemistry. *Anat. Rec. (Hoboken)*, **294**, 1825–1833.
83. Molday, R.S. and MacKenzie, D. (1983) Monoclonal antibodies to rhodopsin: characterization, cross-reactivity, and application as structural probes. *Biochemistry*, **22**, 653–660.
84. Hicks, D. and Molday, R.S. (1986) Differential immunogold-dextran labeling of bovine and frog rod and cone cells using monoclonal antibodies against bovine rhodopsin. *Exp. Eye Res.*, **42**, 55–71.